Contents

4 Photon Beam **2**

4.1 Choice of technique . . . 3
4.1.1 Compton back-scatter . . . 4
4.1.2 Tagged bremsstrahlung . . . 6
4.1.3 Coherent bremsstrahlung . . . 7
4.2 Photon source . . . 8
4.2.1 Essential features . . . 10
4.2.2 Use of collimation . . . 12
4.2.3 Choice of radiator . . . 19
4.2.4 Crystal quality . . . 21
4.2.5 Crystal thickness . . . 25
4.2.6 Crystal mount . . . 28
4.2.7 Crystal alignment and monitoring . . . 30
4.2.8 Crystal lifetime . . . 31
4.3 Electron beam . . . 33
4.3.1 Beam polarization . . . 35
4.3.2 Beam emittance . . . 36
4.3.3 Electron beam line optics . . . 38
4.3.4 Electron beam dump . . . 41
4.3.5 Beam containment and shielding . . . 41
4.4 Tagging spectrometer . . . 42
4.4.1 Specifications . . . 42
4.4.2 Magnet . . . 43
4.4.3 Spectrometer Optics . . . 48
4.4.4 Tagger detectors . . . 50
4.4.5 Beam dump optics . . . 53
4.5 Polarimetry instrumentation . . . 53
4.6 Operating beam intensity . . . 55

Chapter 4

Photon Beam

One of the unique opportunities presented by a CEBAF upgrade to energies of 12 GeV and beyond is the possibility of generating high-intensity continuous photon beams for high-energy photoproduction experiments. In this regime, photon beams represent an interesting extension to the meson spectroscopy program that has been actively pursued using beams of pseudoscalar mesons at hadron accelerator laboratories: with high energy photons one has essentially a beam of *vector* mesons. It is difficult, in fact, to conceive of any other way to obtain such a vector beam.

The requirements for photon beam energy and polarization were described in Chapter **??**. This chapter describes a design for a real photon source that meets these requirements. Starting with a beam of monochromatic electrons, it provides an intense beam of high-energy photons with an energy spectrum that is dominated by a single peak. A significant fraction of the total power in the beam is concentrated inside this peak, which has a width of less than 10% f.w.h.m. At a fixed electron beam energy E_0, the peak energy of the photon beam can be varied anywhere up to 90% E_0 simply by rotating a crystal. The photon spectrum inside the intensity peak has a large degree of linear polarization. The precise energy of an individual photon inside the peak is determined ("tagged") from the momentum of the recoil electron measured in a dedicated "tagging" spectrometer. The design is formed around the expected parameters for the CEBAF beam following the energy upgrade to 12 GeV, although nothing prevents its operation at lower energies before the time that 12 GeV beams are available.

This chapter begins with a survey of the techniques for producing high-energy photons that were considered in the development of this design, and the reasons for the choice of coherent bremsstrahlung. The coherent bremsstrahlung source is then described in greater detail, followed by a discussion

of the requirements that the design places on the electron beam that feeds the source. The tagging spectrometer design is described next, and the chapter concludes with a discussion of the considerations that govern the choice of beam intensity for particular measurements.

4.1 Choice of technique

Two basic methods have been considered for producing photons of the highest possible energy, flux and polarization from electrons of $E_0 = 12\ GeV$. The methods are bremsstrahlung and Compton scattering of light. Both are well-established methods of producing photon beams. Both techniques are actually described by the same Feynman diagrams, shown in Fig. 4.1. In the case of Compton scattering the incoming photon is real, whereas it is virtual for the case of bremsstrahlung.

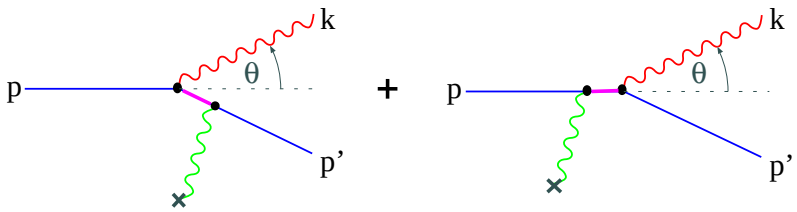

Figure 4.1: Generic diagrams for hard photon production from a high energy electron beam. The symbol × represents either a static charge distribution, in the case of virtual photons in the initial state (i.e. bremsstrahlung), or an optical cavity, in the case of real photons in the initial state (i.e. Compton scattering).

Each of these techniques has its own limitations and advantages. In order to be suitable for GlueX, the photon source must be capable of producing photons of energy at least 80% E_0, $(9\,GeV)$. The photon beam should have linear polarization. The energy resolution for individual photons in the beam should be as high as possible, *i.e.* on the order of the energy spread of the electron beam itself. It should be capable of producing intensities up to 10^8/s. The contamination of the beam with photons outside the desired energy band should be as low as possible. It is also important that the source be reliable and require a minimum of down-time for maintenance. The suitability of each approach is discussed below in the light of these criteria.

4.1.1 Compton back-scatter

A Compton source begins with a beam of visible or ultraviolet light, typically from a laser that is aligned to intersect the incident electron beam at close to 180°. Some of the photons undergo Compton scattering with the beam electrons. In the lab frame, the scattered photons come out in a narrow cone about the incident electron direction and carry a significant fraction of the electron energy.

The basic design of the Compton back-scatter source for this study was put forward by C. Keppel and R. Ent [1]. The design entails the use of a four-mirror high-gain cavity pumped by a 10 kW argon-ion laser putting out 2 ps pulses at a frequency of 100 MHz. The pulses in the cavity are synchronized so that the light pulses intercept an electron bucket each time they pass through the beam. The total length of the cavity is 2 m with a crossing angle of 1°. Both cavity and electron beam are focused to a tiny spot of 10 μm r.m.s. radius at the crossing point. A small spot size is necessary in order to get as high a scattering rate as possible. The gain of the cavity is 10^4, which is conservative in view of recent advances in mirror technology. The wavelength of the light is 514 nm. The rate spectrum of the back-scattered beam from this source is shown in Fig 4.2a for a 1 μA electron beam at 12 GeV.

From the point of view of flux, this source is marginal. With a few μA of beam and mirror improvements, it might produce 10^8 photons/s in the upper third of its energy spectrum. However, its maximum photon energy of 3.7 GeV is far short of the 80% E_0 needed for GlueX. To remedy this one must decrease the wavelength of the laser beam. This can be done by the use of a frequency-doubling crystal that absorbs the green light from the laser and produces ultraviolet light at 257 nm. Storing this light in a cavity of similar design to that described above yields the back-scatter rate spectrum shown in Fig. 4.2b. The major reason for the drop in rate is the decrease in the cavity gain from 10000 to 250. This is imposed by the diminished reflectivities of mirrors in the UV. Other factors are the inefficiency of the doubling crystal, a factor of two in rate from the doubling itself, and the decreasing Compton cross section with energy. The maximum photon energy is still under 50% E_0 and the flux is three orders of magnitude below the desired rate.

In order to reach photon energies of 80% E_0, initial photons of 20 eV are needed. The brightest source of these would be a synchrotron light source or a free electron laser (FEL). Mirrors that operate at these wavelengths typically have reflectivities around 70%. With these one could conceive of a scheme that uses a wiggler to extract energy from the 12 GeV beam before it enters the dump. This light would have the same time structure as incident beam,

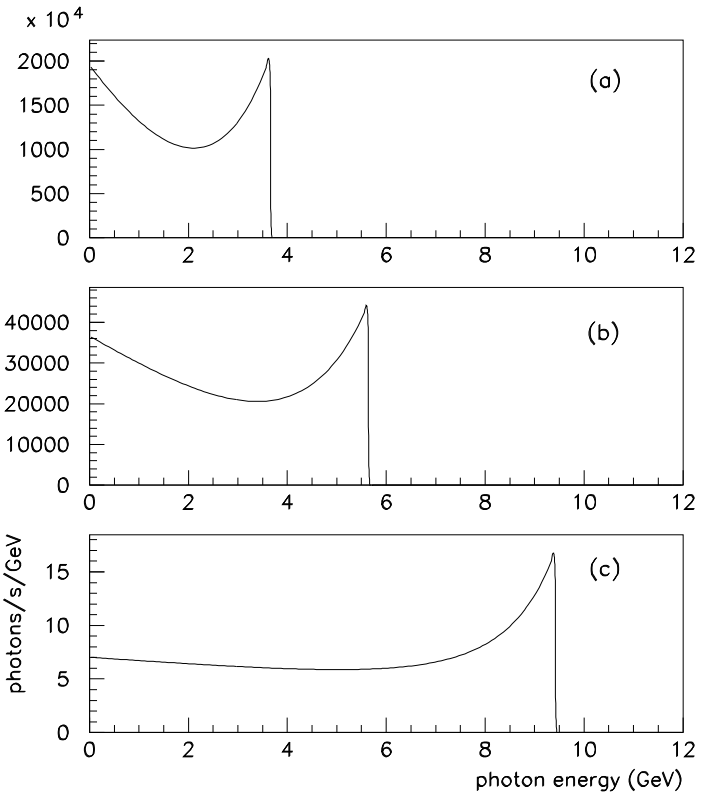

Figure 4.2: Photon energy spectrum from the Compton back-scatter source described in the text and a 12 GeV electron beam at 1 μA. (a) cavity of gain 10000 driven by a 10 kW Argon-ion laser (514 nm) at 100 MHz. (b) cavity of gain 250 driven by 3 kW frequency-doubler (257 nm) pulsed at 100 MHz. (c) cavity of gain 1 driven by a hypothetical FEL source operating at 20 eV with the same time structure as CEBAF beam, peak power 1 kW.

and so it could be reflected back and made to cross the incident beam at a small angle for a Compton back-scatter source. An indication of the level of flux that could be achieved with such a source can be obtained by using the laser cavity model described above, setting the gain to 1, the wavelength to 62 nm, and assuming 1 kW peak (1 W average) of synchrotron light. The back-scatter rate is shown in Fig 4.2c. This plot shows that even if the full

power of a 1 μA on a 12 GeV beam were converted into 20 eV photons and back-scattered from the incoming beam, the rate would still fall far short of the requirements for GlueX.

From the point of view of polarization, the Compton back-scatter source would be ideal. The polarization of the back-scattered beam is controlled by that of the laser, and can be essentially 100%. This source is also virtually background-free because the spectrum below any desired cutoff can be eliminated by collimation. The energy of the remaining beam can be measured to within the resolution of the electron beam by tagging. However the the combination of sufficient energy and sufficient flux for the purposes of the GlueX experiment in Hall D cannot be achieved using this source.

4.1.2 Tagged bremsstrahlung

A bremsstrahlung source consists of a thin piece of material (the radiator) that is placed in the electron beam and converts part of the energy of the beam into bremsstrahlung radiation. Bremsstrahlung offers the only practical way, starting with an electron beam at cebaf energies, to produce a photon beam with a significant flux in the vicinity of the end point. It produces a naturally collimated photon beam with a characteristic angular spread of m/E_0. This allows the low emittance of the cebaf beam to be effectively transfered into the secondary photon beam.

Bremsstrahlung does not suffer from the kind of flux limitations that were encountered in the examination of Compton back-scatter sources. The radiator thickness must be kept below 1% of a radiation length in order to maintain good energy resolution in the tagger. Keeping the thickness below 10^{-3} radiation lengths ensures that multiple scattering in the radiator does not significantly broaden the divergence angle of the photon beam. A 10^{-3} radiator and 1 μA of electrons would produce much more than sufficient flux for GlueX.

A bremsstrahlung source is, however, deficient in some other respects. Averaged over the bremsstrahlung cone, the photon beam has zero linear polarization. Circular polarization can be achieved by polarization transfer from a polarized electron beam, but for the purposes of GlueX it is linear polarization that is desired. A bremsstrahlung source also suffers from a large low-energy flux in the beam. The power spectrum of a bremsstrahlung beam is approximately uniform from zero up to the energy of the incident electrons. This means that an experiment that uses the high-energy part of the beam must operate in a background of low-energy photons that are many times more frequent. The tagger is helpful in eliminating many of the false starts in the

detector that arise from the background, but this technique becomes ineffective at rates above a few 10^7 tagged photons/s. For the typical experiment using tagged bremsstrahlung and open detector geometry, background from low-energy beam particles limits the rate at which the experiment can run to less than $5 \cdot 10^7$ tagged photons/s. The goal for GlueX pushes that limit to 10^8/s by employing tagged *coherent* bremsstrahlung.

4.1.3 Coherent bremsstrahlung

The source described in the previous section meets most of the requirements for GlueX, but is deficient in the areas of polarization and backgrounds. Both of these deficiencies can be remedied by replacing the conventional amorphous or polycrystalline radiator with a thin mono-crystalline wafer. At special settings for the orientation of the crystal, the atoms in the radiator can be made to recoil together from the radiating electron. When they do this they produce a coherent enhancement at particular energies in the radiation spectrum, which correspond to the reciprocal lattice vectors of the crystal. The kinematics are such that a randomly oriented lattice vector would make a tiny peak located up at the end point of the energy spectrum, where the coherent gain factor is negligible. By careful orientation of the crystal, however, one of the lattice vectors can be aligned with the favored kinematics for bremsstrahlung, at which point its coherent peak appears well below the end point, and its coherent gain can be large enough that it contributes a large fraction of the total radiated power.

This is illustrated in Fig. 4.3. This plot shows the intensity (dP/dE) or power spectrum of the coherent bremsstrahlung beam after collimation. The sequence of secondary peaks above the primary correspond to integral multiples of the fundamental reciprocal lattice vector and so they are always present. By careful choice of orientation angles it is possible to suppress all other vectors and isolate just one primary peak in the enegy band of interest, as shown in the figure. By a small rotation of the crystal, the position of the peak can be moved from one end of the spectrum to the other. Note that the coherent peaks appear as enhancements on top of the incoherent bremsstrahlung continuum.

Unlike those from the incoherent process, coherent bremsstrahlung photons have significant net linear polarization in the plane given by the beam direction and the crystal lattice vector. This polarization is enhanced by collimating the photon beam below its intrinsic angular spread, as discussed in the next section. The loss in flux from collimation can be recovered by increasing the electron beam current. As will be shown in the following section, even in the

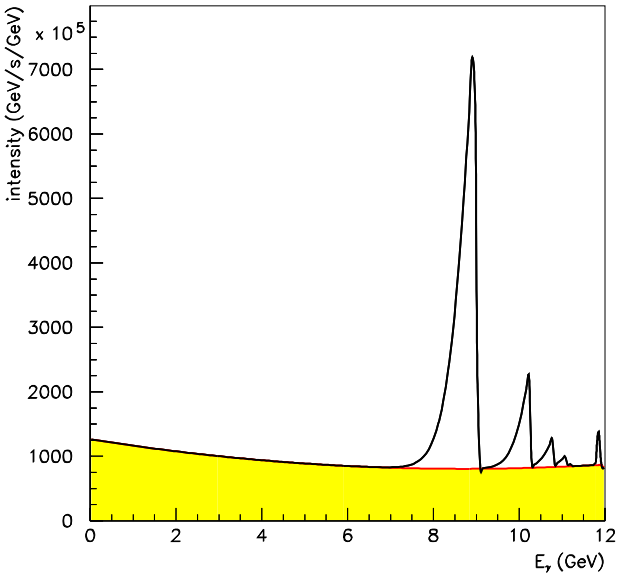

Figure 4.3: Photon power spectrum from an oriented diamond radiator. The y axis is dP/dE with power P expressed in GeV/s and E in GeV. The radiator thickness is 10^{-4} radiation lengths and the electron beam current is 1 μA. Shown is what emerges after the photon beam passes through a collimator 3.4 mm in diameter located 80 m downstream from the radiator.

case of very thin crystals and severe collimation, quite modest electron beam currents are needed to produce the required photon flux.

The use of coherent bremsstrahlung improves the background conditions of the beam by enhancing the spectral intensity in the desired energy band relative to the incoherent continuum. For measurements that do not require polarization, a crystal radiator can be used without collimation to reduce the low-energy beam background for a given rate of tagged photons. Where polarization is required, coherent bremsstrahlung is indispensable.

4.2 Photon source

A horizontal plan view of the photon beam line is shown in Fig. 4.4 with the major components labeled. The electron beam enters the figure from below ground at the left and is bent into the horizontal plane to enter the tagger

building. There it passes through two small dipoles to impinge upon the bremsstrahlung radiator. After its exit from the radiator, the electron beam passes into the tagging spectrometer where the primary beam is bent in the direction of the electron beam dump. The radiator crystal is thin enough that the average energy loss by the electrons in traversing the radiator is less than the intrinsic energy spread of the incident beam. Those electrons which lose a significant fraction of their initial energy inside the radiator do so by emitting a single bremsstrahlung photon. These degraded electrons are bent out of the primary beam inside the tagger magnet and exit the vacuum through a thin window, passing through air for a short distance to strike the focal plane of the spectrometer. The primary electron beam is contained inside vacuum all the way to the dump.

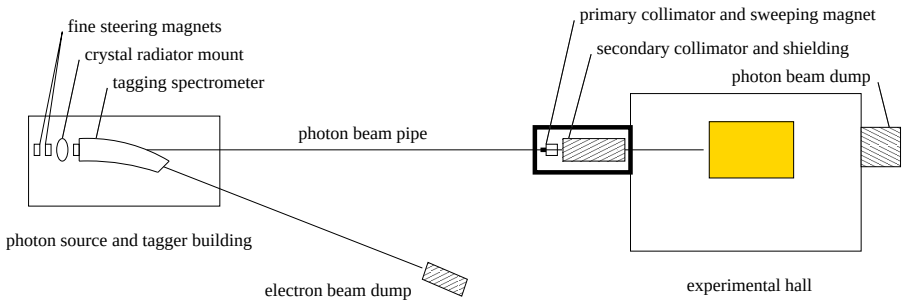

Figure 4.4: Schematic plan view of the photon beam line, shown in the horizontal plane as viewed from above. The objects in this figure are not drawn to scale.

The photons that are produced in the radiator pass through a small hole bored in the return yoke of the tagger magnet in the forward direction. They then pass into an evacuated photon beam pipe and travel to the experimental hall. Just before entering the hall the photon beam passes through a system of collimators and sweeping magnets. They are housed in a separate enclosure for shielding purposes. The primary collimator is first. It defines the part of the photon beam that is allowed to reach the target. Debris from interactions along the inside surface of the collimator bore forms a halo around the photon beam that exits the primary collimator. The charged component of the halo is deflected away from the beam axis by a dipole "sweeping" magnet just downstream of the collimator. A secondary collimator follows the sweeping magnet to stop the deflected shower particles and block the halo of secondary photons generated by the first collimator. The secondary collimator is of a larger diameter than the primary and so sees a reduced rate of secondary interactions on the inner surface of the hole. What new showers are generated there are

cleaned up by a second sweeping magnet. The beam then passes through a block of shielding material into the experimental hall. This triple-collimation system is similar to the setup at the SLAC coherent bremsstrahlung beam line [2].

The collimated photon beam, now only a few mm in diameter, is delivered to the experimental target. After passing through of order 3% radiation lengths of target, the photon beam passes through the detector and into the photon beam dump at the back of the hall. Based upon a design upper limit of 60 kW (5 μA at 12 GeV) being delivered to the electron beam dump, the total power in the photon beam is not more than 1.5 W in the experimental hall and not more than 15 W in the collimator enclosure.

4.2.1 Essential features

The adjective 'coherent' in coherent bremsstrahlung does not indicate that the photons in the beam are in a coherent state, as is light from a laser. Rather it refers to the coherent effect of multiple atoms in a crystal lattice in absorbing the recoil momentum from a high energy electron when it radiates a bremsstrahlung photon. In X-ray spectroscopy one encounters the same thing in the Mössbauer effect, except in that case the chief physical consequence is the disappearance of the recoil Doppler shift from the photoabsorption/emission spectrum. Here the chief consequence is the enhancement of bremsstrahlung at those particular kinematics for which the recoil momentum matches one of the reciprocal lattice vectors of the crystal.

Another useful way to view the process of coherent bremsstrahlung is as virtual Compton scattering. To the high energy electron, the atoms in the radiator appear as clouds of virtual photons. For a disordered radiator material, the virtual photon spectrum is given simply by the atomic form factor squared, averaged over the different species in the material. If the radiator is a single crystal, however, the atomic form factor gets multiplied by the form factor of the crystal, which in the ideal case looks like a series of delta-functions located at the sites of the reciprocal lattice. In effect, the crystal provides a set of virtual laser beams, each one a standing wave tuned to a specific reciprocal lattice vector. In this view the process of hard bremsstrahlung is seen to be the same as Compton back-scattering of laser light. For a more detailed discussion of the physics of coherent bremsstrahlung there are a number of good references [2, 3, 4, 5].

The use of Compton back-scattering of laser light as a photon source was earlier noted as ruled out by the limitation of high-power lasers and cavities to wavelengths above 100 μm. The characteristic wavelength of the crystal

photons is a few Angstroms, three orders of magnitude shorter. In this case, 180° scattering would result in essentially 100% of the electron beam momentum being transferred to the photon in the lab frame. However, the Compton cross section contains a factor of $1/(\vec{q}\cdot\vec{p})^2$ where $\vec{q}$ is the virtual photon momentum and $\vec{p}$ is that of the electron, which strongly favors incident photons with $\vec{q}$ nearly orthogonal to $\vec{p}$. With reciprocal lattice vectors pointing in almost every direction, only those nearly perpendicular to the beam contribute appreciably to the scattering rate. This fact applies equally to ordinary bremsstrahlung; in fact, to a first approximation the bremsstrahlung spectrum from a single crystal is the same as from a disordered radiator. The reason is that, if the sum over crystal momenta were replaced with a continuous integral, one would recover the ordinary bremsstrahlung result for isolated atoms. Beyond a few unit cells from the origin in reciprocal lattice space, the atomic form factor and kinematic factors become slowly varying on the scale of the lattice spacing, and the sum becomes indistinguishable from the integral. Besides that, the uncertainty principle requires that atoms localized at the sites in a crystal undergo fluctuations about their mean position. This has the effect of attenuating the discrete peaks in the crystal form factor at progressively higher-order crystal momenta, eventually washing them out and filling in the gaps between them, so that the sum deforms smoothly into the integral at high momentum transfer. Hence, the sum over crystal indices that yields the final photon spectrum can be separated into two parts: a discrete sum over a limited set of small crystal indices and an integral over the continuum of momentum transfer values beyond. The latter appears in the coherent bremsstrahlung beam as an ordinary $1/k$ bremsstrahlung spectrum, while the former appears as a set of peak structures superimposed upon it. The $1/k$ continuum, referred to as the incoherent component, is invariant as the crystal is rotated, whereas the coherent peaks change in position and intensity, depending on crystal orientation.

A typical coherent bremsstrahlung spectrum is shown in Fig. 4.5. The distinction between incoherent and coherent components in the figure is artificial; it is there to show the part of the spectrum that shifts as the crystal is rotated. The vertical scale in the figure gives the photon rate for the given beam current and crystal thickness. Note that the intensity of the incoherent background is less than what would be obtained with an amorphous carbon radiator of the same thickness, because a part of the momentum transfer integral in the Bethe-Heitler formula has been moved into the discrete sum and contributes to the coherent part. The radiation length of diamond is actually an average over all orientations of the crystal. In the calculation for Fig. 4.5 the leading 400 lattice sites were included in the discrete part of the calculation, although

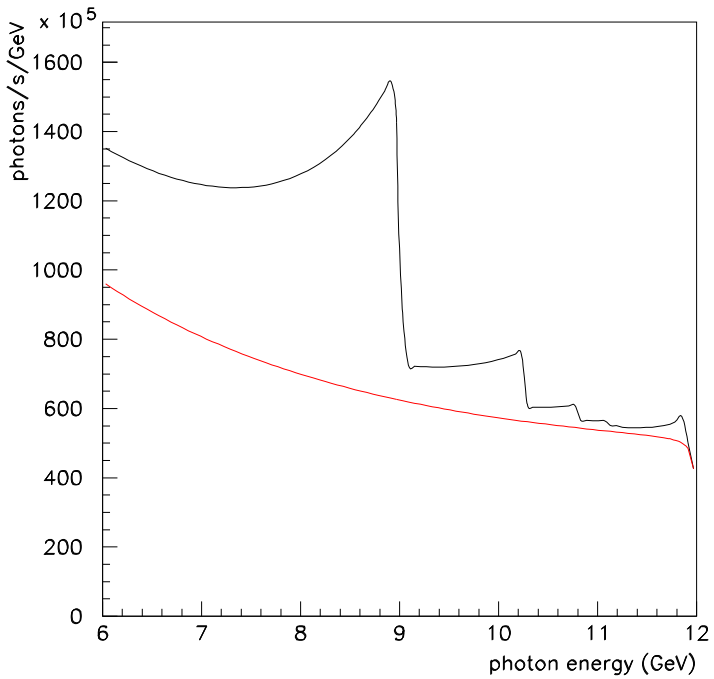

Figure 4.5: Uncollimated coherent bremsstrahlung spectrum, calculated for a diamond crystal radiator 15 μm thick and a 1 μA electron beam of 12 GeV energy. Typical values are used for beam emittance and crystal mosaic spread.

it can be seen that, at the chosen crystal orientation, only two or three of them contribute with sufficient intensity to be individually visible in the spectrum.

4.2.2 Use of collimation

The presence of the large incoherent continuum in Fig. 4.5 presents a significant handicap to a photoproduction experiment. Not only do the continuum photons produce background in the detector, but they diminish the polarization of the beam. The entire beam polarization appears in the coherent component; the underlying incoherent flux only serves to dilute the polarization. There is another difference between the two components that allows them to be separated to some extent. The kinematics of bremsstrahlung confines most of the intensity of the photon beam to forward angles within m/E radians of the incident electron direction. This is true both for the incoherent and coherent

components. In the lab this is a small angle, but in the rest frame of the electron-photon system it subtends all angles in the forward hemisphere. The difference lies in the fact that a peak in the coherent component corresponding to a single reciprocal lattice vector has two-body kinematics, so there is a well-defined relation between the emission angle and the energy of the emitted photon in the lab: emission at 0° yields a maximum energy photon, with energy decreasing with increasing angle. This accounts for the shape of the coherent peaks in Fig. 4.5, with the sharp right-hand edge corresponding to 0° emission and the tail to lower energies corresponding to emission at higher angles.

The incoherent component, because it comes from a sum over momentum transfers at all angles, has essentially no correlation between photon energy and emission angle. This means that collimating away all photons beyond some angle $\theta_{max} < m/E$ uniformly attenuates the incoherent spectrum at all energies, whereas it preserves all of the coherent photons from the maximum energy for the given peak down to some cutoff. The kinematic relations for coherent bremsstrahlung are as follows,

$$\theta^2 + 1 = \left(\frac{1-x}{x}\right)\left(\frac{x_{max}}{1-x_{max}}\right) \tag{4.1}$$

$$x_{max} = \frac{2\vec{p}\cdot\vec{q}}{2\vec{p}\cdot\vec{q} - m_e^2} \tag{4.2}$$

where x is the photon energy in units of the incident electron energy and θ is the lab emission angle of the photon relative to the incident electron momentum axis, in units of m/E .

The effects of collimation are demonstrated in the calculated spectra shown in Fig. 4.6. First, note that the collimation angles are very small, which requires a long flight path of order 100 m in order that the collimator can be larger than the intrinsic beam spot size, otherwise the collimator is cutting in transverse coordinate instead of in angle. This distance is, in fact, a sensitive function of the electron beam emittance from the machine, and must be increased in inverse proportion to the beam emittance if the effectiveness of collimation is held constant. This issue, along with the associated demands placed on beam alignment and position stability, are taken up in more detail in the following section on the electron beam line.

Second, note that the cut imposed on the coherent peak by collimation does not produce a perfectly sharp edge as would be expected from two-body kinematics. This is because the collimator cuts on radius at some fixed distance which translates into a cut on emission angle only in an approximate way.

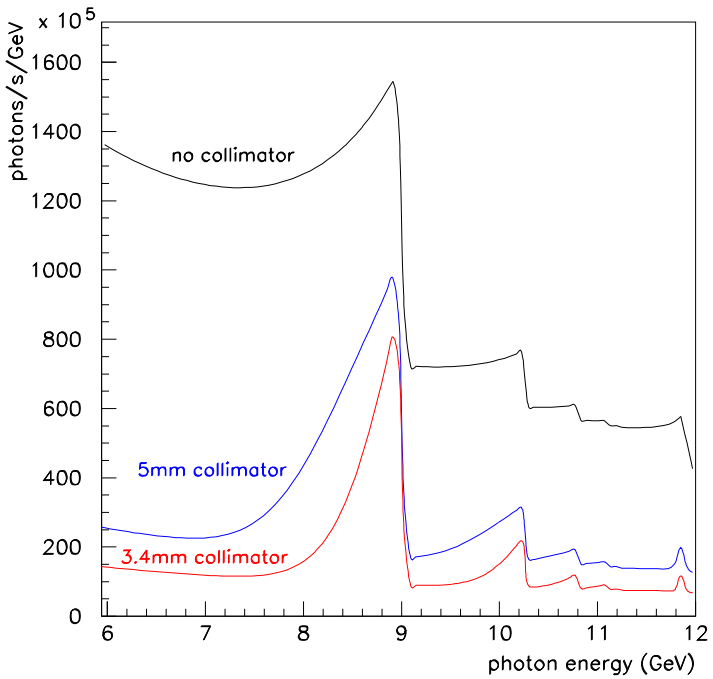

Figure 4.6: Coherent bremsstrahlung spectrum, calculated under the same conditions as in Fig. 4.5 , after collimation. The upper curve is the uncollimated spectrum from Fig. 4.5. The middle curve corresponds to a 5 mm diameter collimator placed 80 m downstream of the radiator, or approximately $0.75\,m/E$ in collimator half-angle. The lower curve corresponds to a 3.4 mm collimator in the same position, approximately $0.50\,m/E$. For the 3.4 mm collimator there are approximately $3.3 \times 10^7 \gamma/s$ in the primary peak for a nominal electron beam current of 1 μA and crystal thickness of 15 μm.

Thus the curves in Fig. 4.6 are labeled by their collimator size and distance individually, rather than their ratio, which is the nominal collimation angle. Multiple scattering by the electron in the radiator prior to emission, and beam spot size and divergence are the major contributors to the error involved in translating a collimator radius into a cut on emission angle. All of these effects have been incorporated into the analytical calculation of the yields from a collimated coherent bremsstrahlung source that has been used in preparing this report. Crystal imperfections, which amount to an intrinsic spread in the direction of the incoming virtual photon, are also taken into account in the

calculation.

Third, note that the relatively weak collimation at 5 mm reduces the incoherent background without significantly affecting the coherent flux near the maximum, and thereby almost doubling the polarization of the beam at the peak relative to the uncollimated case. Further reducing the collimator diameter continues to narrow the peak and reduce the incoherent flux relative to the peak, albeit at some cost in peak intensity.

The 3.4 mm collimator diameter has been chosen for this design because it provides for a maximum reduction in the incoherent flux while transmitting 95% of the coherent flux at the peak. Most of the total photon beam energy coming from the crystal is absorbed by the collimator. For this reason the collimator is located in a separate enclosure outside the experimental hall, and must be surrounded by a considerable amount of shielding. The peak in Fig. 4.6 for a 3.4 mm collimator contains 33M photons/s for an electron beam current of 1 μA, which will be increased by a factor of 3 for full-intensity running of the GlueX experiment in Hall D.

Fourth, note that the rate seen in the focal plane of the tagging spectrometer corresponds to the upper curve in Fig. 4.6, regardless of the collimation. This means that collimating the bremsstrahlung beam increases the rate in the tagger focal plane relative to what is seen at the detector. For full-intensity running at 10^8 photons/s on target in the coherent peak, Fig. 4.6 implies a rate of 240 MHz in the focal plane within a 600 MeV window around the peak. Combining this rate with the beam pulse spacing of 2 ns leads to an accidental tagging rate of about 50% and to a fraction of ambiguous tags of 40%. Even with ideal electronics the per-second yield of single-tag events is close to saturation at this intensity. The detector and tagging spectrometer design are based upon a maximum rate of 10^8 photons/s on target and 400 MHz per GeV in the tagger. A novel focal plane design is currently under study, to be discussed below in section 4.4, which may enable the focal plane rate to be reduced by about a factor of two without any decrease in the collimated flux.

The linear polarization of the photons in the coherent peak is shown in Fig. 4.7 as a function of the energy of the electron beam. This figure demonstrates why it is essential to have electrons of as high energy as possible, even though photon energies of no more than 9 GeV are required. The intensity of the coherent peak, not shown in the figure, has a similar dependence on the electron beam energy in this region.

Shown in Fig. 4.8 is the linear polarization of the photon beam *vs* photon energy for fixed electron beam energy. The dashed curves show how the maximum polarization in the primary peak varies as the peak energy is changed by rotating the crystal. The polarization in all cases is zero at the end-point.

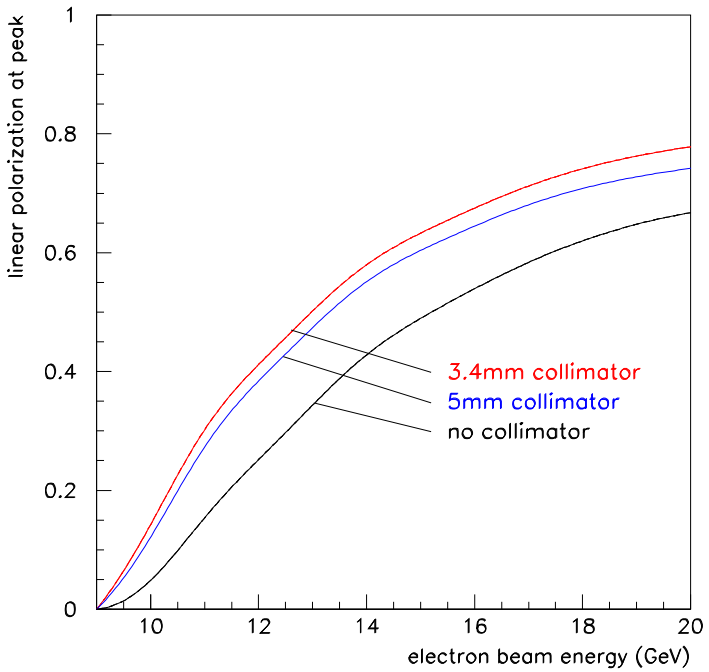

Figure 4.7: Linear polarization in the coherent bremsstrahlung peak as a function of electron beam energy keeping the energy of the coherent peak fixed at 9 GeV. The calculation is performed under the same conditions as in Fig. 4.6.

Without collimation it rises as $(E_0 - k)^2$, one power coming from the intensity of the coherent peak relative to the incoherent component, and the other from the intrinsic polarization of the coherent photons. Collimation allows one to essentially isolate the coherent component, so that the polarization available to the experiment rises from zero at the end-point in a linear fashion. The dashed curves in Fig. 4.8 demonstrate this point.

In order to obtain the full polarization enhancement from collimation, it is necessary to have a distance between the radiator and collimator on the order of 100 m. This distance scale is set by the requirement that the collimator aperture must be large compared to the virtual electron beam spot on the collimator but small compared to the actual photon spot size. The virtual electron beam spot is defined as the profile that the electron beam would have at the entrance to the collimator if it were allowed to propagate freely instead of being bent into the beam dump.

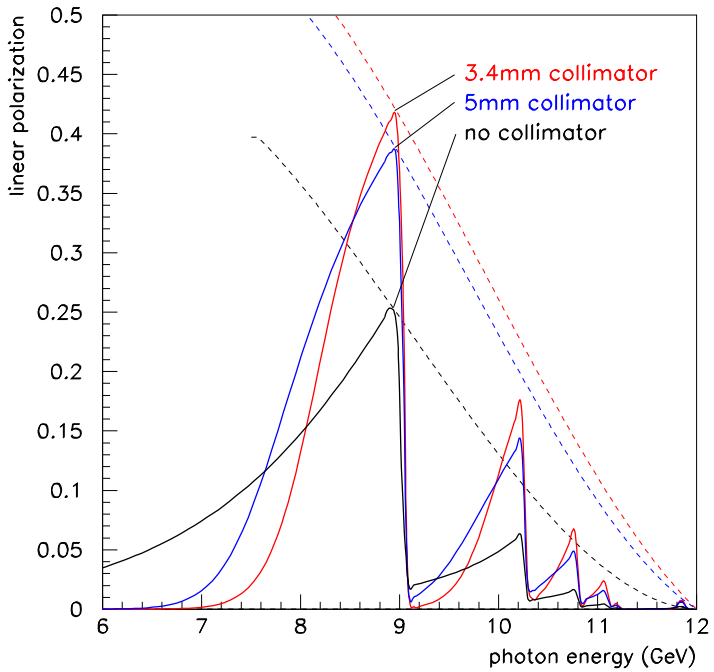

Figure 4.8: Linear polarization of the coherent bremsstrahlung beam for a fixed electron beam energy of 12 GeV, calculated under the same conditions as in Fig. 4.6. The dashed lines indicate the trajectory of the peak polarization as the peak energy is swept across the focal plane by rotating the crystal.

The size of the virtual spot at the collimator is determined by the beam emittance combined with an upper limit of 20 μr on the angular spread of the electron beam at the radiator. The latter value was chosen to match the spread in the beam incidence angle to the mosaic spread of the crystal because it is the combination of the two that limits the definition of the coherent peak. Taking this value together with an emittance of 10^{-8} $m \cdot r$, which has been projected for the CEBAF beam at 12 GeV leads to a virtual spot size of 0.5 mm r.m.s. (1.2 mm f.w.h.m.). Note that this scale does not depend on the radiator-collimator distance. The size of the real photon spot is given by one characteristic angle m/E which defines a circle on the collimator containing approximately 50% of the total photon intensity. The real spot size is proportional to the radiator-collimator distance. At a distance of 80 $m$the ratio of spot sizes is 6, sufficient to allow collimator apertures that satisfy both

of the above inequalities.

Fig. 4.9 shows the peak polarization of the beam as a function of radiator-collimator distance for a coherent peak at 9 GeV. In this calculation the collimator diameter is held constant at 3.4 mm to make sure that the virtual beam spot of 1.2 mm f.w.h.m. is well-contained within the aperture, which is the main condition for effective collimation. At zero distance the collimator has no effect except to attenuate the beam, and so the uncollimated polarization from coherent bremsstrahlung is obtained. At 100 $m$separation distance the polarization enhancement from collimation has saturated. The design for GLUEχ calls for a radiator-collimator distance of approximately 80 m. However from the figure one can see that the performance of the photon source is not a very sensitive function of this variable.

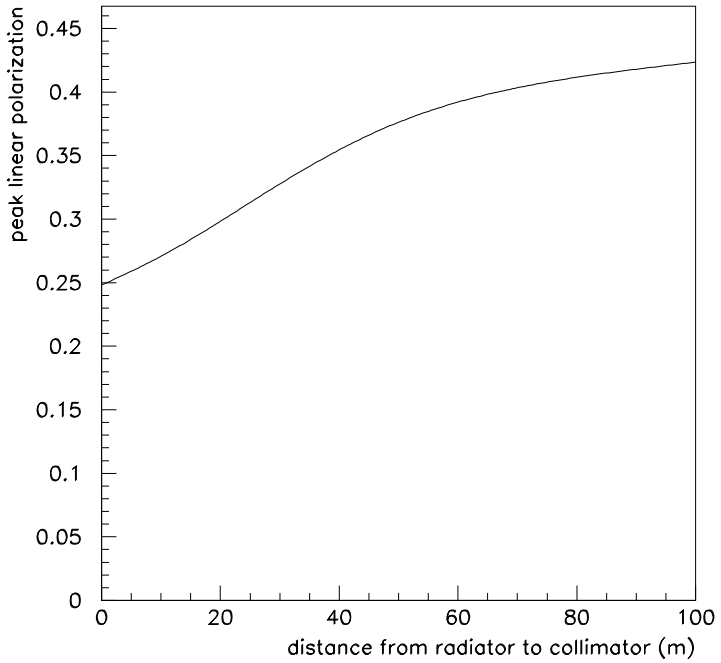

Figure 4.9: Maximum polarization *vs* radiator-collimator distance for a coherent peak at 9 GeV. The collimator diameter is held fixed in this calculation to keep a constant ratio between the sizes of the virtual electron spot and the collimator.

crystal	best reciprocal vector	$P/P_{diamond}$
diamond	2,-2,0	1.00
beryllium	0,0,2	0.86
boron	2,0,8	0.38
silicon	2,-2,0	0.19
Be_2C	2,2,0	1.10

Table 4.1: Figure of merit for various materials that might be used as a coherent bremsstrahlung radiator. This table is reproduced from Table 2 in Ref. [3].

4.2.3 Choice of radiator

The ideal radiator would be a layered structure with strong transverse fields that alternate between layers spaced about 50 nm apart, thus simulating the standing wave in a cavity driven by a 15 eV laser. While it is possible to construct ordered materials with unit cells as large as this, the self-shielding of atoms means that beyond the atomic length scale the residual fields are comparatively weak. Hence heterogeneous structures are not viable for use as a coherent radiator. Since the strong fields inside a solid are revealed at the atomic scale, the first requirement for a good radiator is that the unit cell be compact and closely packed. The best radiators are those with the smallest unit cells because these provide the best match between the atomic and the crystal form factors. This match is best for the light elements, and essentially prohibits the effectiveness of any materials heavier than carbon. An extensive survey of possible radiator materials is presented in Ref. [3]. In Table 4.1 is shown the figure of merit that those authors report for favored crystalline materials. The figure of merit is the product of the atomic times the crystal form factor evaluated at the leading peak, normalized to the value for diamond.

Table 4.1 shows that the list of viable materials for a crystal radiator is relatively short. Silicon would be an excellent choice from the point of view of price and fabrication, but unfortunately it is far inferior in terms of performance. Beryllium carbide is not a material that is familiar to the crystal growth industry, and nothing is known at present concerning its suitability for the growth of single crystals of large area. In general compound materials are more susceptible to radiation damage than are pure elements, which would argue in favor of diamond and beryllium metal. These two materials

are comparable in terms of their performance.

Most of the experience to date with coherent bremsstrahlung has been with diamond radiators. Extensive expertise with large diamond crystals, such as would be required for the production of coherent bremsstrahlung radiators, already exists within the gem industry. However such capabilities are typically treated in that highly competitive business as sensitive corporate information, particularly as they pertain to the creation of large gem-quality synthetics. Researchers at the University of Glasgow have established contacts within the gem industry for procuring single-crystal diamonds of high quality and large surface area [6]. The techniques used for selecting and assessing the quality of the diamonds are discussed in the next section.

In general terms, diamonds are classified as type I or type II, where type II have been subjected to greater stresses during their formation than type I. Commonly, type II exhibit substantial plastic deformation. Diamonds are also classified according to the form in which nitrogen atoms are present in the crystal lattice. In type *a* the nitrogen is aggregated into clusters of atoms, whereas in type *b* the nitrogen is almost uniformly distributed throughout the crystal. For coherent bremsstrahlung radiators, type Ib diamonds are the most suitable. Unfortunately, type Ib natural diamonds are very rare and probably the most reliable source of Ib diamonds will be synthetics. At present synthetic diamond mono-crystals typically have nitrogen concentrations around 100 ppm.

Synthetic diamonds are made using either vapor deposition (CVD) or high pressure high temperature (HPHT) techniques. CVD diamonds have an extensive mosaic and are unsuitable for coherent bremsstrahlung. However HPHT synthetics look very promising, and the Glasgow group have recently acquired a $5 \times 5\ mm^2$ synthetic diamond less than 18 μm thick which has a [100] orientation. It produces a very good coherent bremsstrahlung spectrum and X-ray measurements show it has rocking curve widths of less than 10 μr, quite close to the ideal value for diamond.

Beryllium is another material that might be used as a crystal radiator. Beryllium metal is widely used in industry, being preferred for its high strength-to-weight ratio and robustness, in addition to its transparency to X-rays. Thin films of high-purity beryllium are routinely produced for vacuum window applications, which use some of the same vacuum deposition techniques that would be used for the growth of single crystals. As a radiator material, beryllium is distinguished as the metal with the highest Debye temperature, around 1400°K . The Debye temperature measures the temperature at which the thermal motion of the atoms in the lattice reaches the level of the zero-point motion due to their confinement in the lattice. A high Debye temperature indicates a

stiff crystal lattice, in which the atoms have little liberty to move and so have large momentum fluctuations, as dictated by the uncertainty principle.

A high Debye temperature is important for a bremsstrahlung radiator material for three reasons. First, the cross section for coherent bremsstrahlung from a discrete crystal momentum vector $\vec{q}$ contains a factor $e^{-q^2/4M\theta_D}$ which reflects the fact that position fluctuations of atoms in the lattice diminish the coherent effect. This factor is near unity for the low-order crystal momenta provided that the Debye temperature θ_D is sufficiently large. Second, the Debye temperature is, roughly speaking, a measure of the stability of the crystal structure and hence its capacity to survive significant doses of radiation. Third, the radiator material will inevitably be heated by the beam, and will normally operate in vacuum well above the ambient temperature. A high Debye temperature means that there is a large range of temperatures over which the material may operate without degraded performance as a crystal radiator. The Debye temperature of diamond is about 2200° K.

Past experience has shown that diamond meets all of the requirements for a good crystal radiator. Beryllium remains a second choice, to be investigated further in the case that affordable sources of large-area diamond crystals at some point are no longer available.

4.2.4 Crystal quality

In the calculation of the coherent bremsstrahlung spectrum it is necessary to take into account the fact that even the very best crystals have some dislocations and other defects. Besides locally disrupting the regularity of the crystal, these defects impose stresses which produce small ripples in the crystal planes. If these ripples were amplified, the surface of a crystal would appear like a mosaic of planar regions with approximately parallel surfaces. The scale of deviations from planarity across the face of a single crystal is termed the *mosaic spread* of the crystal. The mosaic spread contributes in the same way as electron beam divergence to the blurring of the exact energy-angle relation for coherent photons.

Besides dislocations, there are other kinds of crystal defects. The presence of foreign atomic species during the crystal growth process can result in the substitution of impurities at some lattice sites, or the formation of voids where impurities tend to collect in clusters of several atoms. In the growth of diamond crystals under conditions of high pressure and temperature, the growth rate is greatly enhanced by the presence of a small amount of nitrogen. Thus it is normal that small amounts of nitrogen impurities should exist even in the best natural stones, as well as in the synthetics created by the HPHT process.

The ideal conditions for growth of a perfect synthetic crystal require pre-existing mono-crystalline diamond with clean planar facets cleaved along the major crystal planes, upon which new layers of carbon are deposited in succession. If conditions are right, the registry of the atoms with the original crystal is preserved over millions of deposited layers, starting from the original seed. In principle, the expansion of the regular lattice should continue to match up perfectly at the boundaries between the different growth surfaces that originated on the facets of the seed, but in practice the strains from small imperfections that occur during the growth process tend to accumulate there, forming recognizable patterns of concentrated defects known as *growth boundaries*. If the stresses grow too large then new strain regions may develop, leading to a more pronounced mosaic pattern in the subsequent layers.

Unfortunately the growth process has proved difficult to control in a reproducible fashion. As a result, out of several dozen stones examined, only one or two may be of sufficient quality for use as a coherent bremsstrahlung radiator for Hall D. The selection process described below was formerly developed by the Glasgow group to supply crystals for the coherent bremsstrahlung source at Mainz, Germany and subsequently for the Hall B source at Jefferson Lab. The requirements for Hall D are very similar to those of Mainz and Hall B, except that the electron beam current will be higher by about an order of magnitude and the crystals will be cut much thinner.

The diamond ingots from the synthetic process are sliced into sections at the laboratory where they are produced. From these, thin wafers of about 100 μm thickness are cleaved along the (1,0,0) axis and provided to the Glasgow group for assessment. The samples are first examined under a microscope with polarized light. Many of the stresses in the crystal lattice can be revealed in this way, particularly those which exhibit plastic deformation. If the diamond appears clear and featureless under polarized light then it is examined with X-rays. Two types of X-ray measurements are performed.

1. Topographs
   A topograph is a real-space image of a diamond formed from X-rays that Bragg-scatter from a particular set of planes in the crystal, as shown in Fig. 4.10a. Using the highly-parallel X-ray beam from the Synchrotron Light Source (SRS) and setting the detector at twice the Bragg angle for a known set of planes for diamond, X-rays of the appropriate wavelength to satisfy the Bragg condition are scattered at a precise angle θ into the detector. The X-ray image formed on the plane of the detector is a simple real-space projection of the crystal, called a *projection topograph*. If the vertical slits defining the X-ray beam are narrowed forming

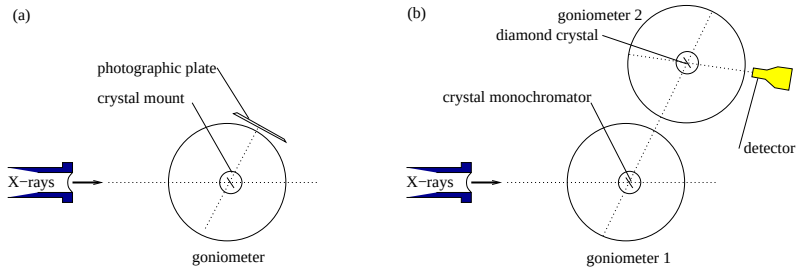

Figure 4.10: Experimental setup for assessment of diamond crystals at the Synchrotron Light Source beam line, configured for topograph measurements (a), and rocking curves (b).

the incident beam into a thin ribbon a few μm wide, then the image at the detector reveals a slice though the crystal, called a *section topograph*. Projection topographs reveal any large-scale imperfections in the crystal. Section topographs can be used to examine the depth profile of imperfections. Topographs sample the whole volume of the crystal. Hence, by measuring projection and section topographs, a 3-dimensional picture of the diamond can be obtained. It is also possible to differentiate between screw and edge dislocations. The topograph image reveals dislocations, growth boundaries and any feature which suppresses or enhances Bragg scattering at the selected angle. In principle, topographs taken at different angles provide independent views of the crystal structure. In in practice, however, the imperfections that are revealed with one set of planes appear in a similar fashion when viewed from other orientations.

2. Rocking curves
   A rocking curve is a plot of Bragg-scattering intensity *vs* angle between the incident X-ray beam and the normal to the crystal planes. A diagram of the setup is shown in Fig. 4.10b. First the broad-band X-ray beam from the SRS is monochromated by scattering at a known fixed angle from a reference crystal, in this case silicon. This beam is then directed at the diamond crystal under study, from which it scatters a second time and is detected. The scattering is appreciable only when the diamond is at just the right angle with respect to the incident beam such that the Bragg condition is satisfied at both crystals. The variation in the scattering intensity with angle as the diamond wafer is rotated through the resonance is called the *rocking curve* for that diamond. A perfect crystal exhibits a rocking curve consisting of a single peak whose width is called the *natural width* and depends on the material. The natural

width for diamond is about $5\,\mu r$. Instead of a single peak, for actual crystals one typically sees a number of peaks spread out over a region in angle over known as the rocking curve width. Rocking curves widths, for a selected set of crystal planes, measure quantitatively how any defects or dislocations distort the crystal lattice. By adjusting the slits it is possible to examine the rocking curve of a region of the crystal or to examine the entire crystal at once. Using rocking curves it is possible to measure how close to ideal is the lattice structure of the diamond being investigated.

Figs. 4.11-4.12 show some of the results that were obtained at the SRS laboratory in Daresbury, England in January, 2002. At the left of the figures is shown a projection topograph taken using the (0,4,0) planes, the second harmonic of the (0,2,0) planes used for coherent bremsstrahlung. At the right is shown the corresponding rocking curve taken in combination with a silicon crystal set to reflect from the (3,3,3) planes at a wavelength of 1 Å. The two diamond wafers had been cut from the same original type Ib stone, with Fig. 4.11 coming from the end close to the seed, and Fig. 4.12 coming from near the middle of the ingot. The topographs are negatives, meaning that the image is dark in regions where the X-ray intensity was largest.

The first thing to notice from the topographs is that both wafers are monocrystalline; there are no regions where X-rays do not scatter. Even so, there are important differences between the two samples. The growth boundaries (the picture-frame pattern) which are visible in Fig. 4.11 spread out and become less pronounced in slice 2 which was taken further from the seed. It is interesting that the strain pattern appears mostly as dark regions rather than light, which indicates stronger scattering in the defects than in the ordered regions, the opposite from what one might naively expect. It should be recalled that both crystals appeared clear and featureless under polarized light at visible wavelengths. The requirement for a diamond radiator useful for Hall D is that the rocking curve width be of the same order of magnitude as the divergence of the electron beam at the radiator, which when folded with multiple-scattering is about 25 μr r.m.s. The conclusion is that slice 2 is a good candidate for use in the GlueX experiment, and that slice 3 is not. Having confirmed the quality of slice 2, it should now be possible for the manufacturer to cut a dozen or more wafers of similar quality from that region of the original stone.

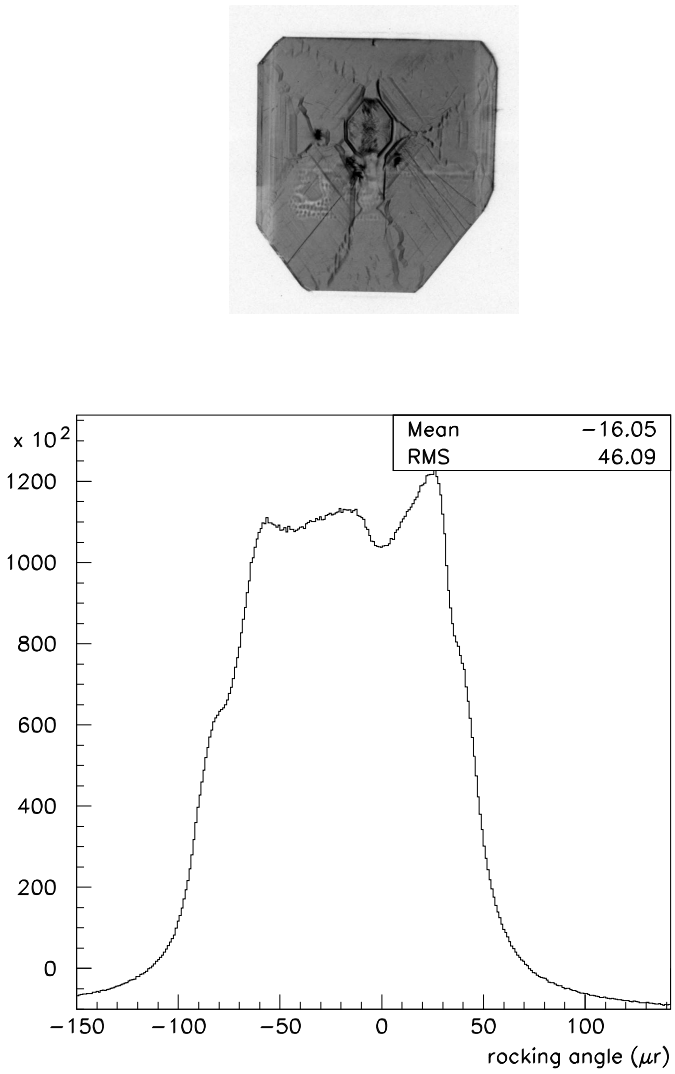

Figure 4.11: Experimental data collected using highly-parallel X-rays from the SRS light source for stone 1482A slice 3 (close to the seed). At the top is shown a projection topograph of the wafer taken using the broad-band X-ray beam and a Polaroid film placed at the angle for reflection from the (0,4,0) planes. The image is a magnified by a factor of 5. The graph shows the rocking curve for the same set of planes, taken using a NaI counter and 1 Å X-rays monochromated by a silicon crystal.

4.2.5 Crystal thickness

The range of permissible thicknesses for a crystal radiator is bounded both from above and below. It is bounded from above by multiple scattering of the

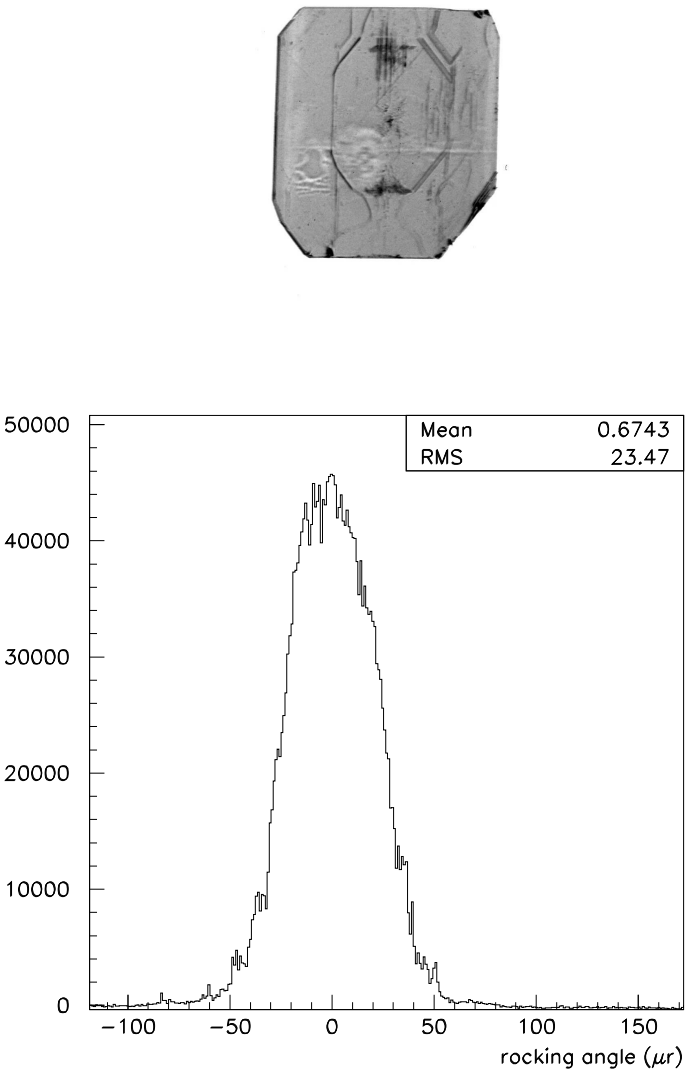

Figure 4.12: Experimental data collected using highly-parallel X-rays from the SRS light source for stone 1482A slice 2 (further from the seed). At the top is shown a projection topograph of the wafer taken using the broad-band X-ray beam and a Polaroid film placed at the angle for reflection from the (0,4,0) planes. The image is magnified by a factor of 5. The graph shows the the rocking curve for the same set of planes, taken using a NaI counter and 1 Å X-rays monochromated by a silicon crystal.

electron beam as it passes through the radiator, which causes the divergence of the incident beam to grow, thereby enlarging the photon beam spot on the collimator face and degrading the degree to which collimation discriminates against the incoherent component in favor of the coherent part. It is bounded from below by the fact that the crystal must have some minimum thickness in order to achieve the full coherent gain. In the calculation of the coherent bremsstrahlung process one begins by assuming an infinite crystal, although practically it is presumed to mean only that the crystal is large compared to some characteristic scale. It is important to identify what the characteristic scale is in this problem in order to know how thin one can make the crystal without hurting performance. In the analogous case of the Mössbauer effect, one can estimate the number of atoms participating in the collective absorption by looking at the emission time of the photon (lifetime of the radiating transition) and asking how many nuclei lie within the envelope of the photon wave packet. In the coherent bremsstrahlung process, the lifetime of the radiating system is given in the lab system by the uncertainty principle and by how far the electron energy deviates from its on-shell value between absorbing the virtual photon and emitting the real one. The latter quantity is almost exactly given by q_z , the virtual photon momentum component along the incident electron axis, which means that the electron travels a distance $\lambda = \hbar c/q_z$ during the interaction. For a given coherent peak at normalized energy x in the photon spectrum, the coherence length is given by

$$\lambda = \frac{2E(1-x)}{xm^2} \tag{4.3}$$

in units of $\hbar c$. From this simple argument one sees that the coherent gain goes linearly to zero at the end-point, a result that is borne out by the full QED calculation. One also sees that the lower limit on crystal thickness imposed by the coherence length depends upon both the electron beam energy and the photon energy. For a 12 GeV beam energy and a 6 GeV coherent photon the coherence length is 18 nm, or about 50 unit cells for diamond. This shows that the coherence length does not impose a practical limit on how thin the radiator should be.

The effects of multiple scattering are best presented by showing the calculated spectra for various radiator thicknesses. In Fig. 4.13 is shown the photon spectrum for a 10^{-4} and a 10^{-3} radiation-lengths radiator to demonstrate the effect. The 10^{-3} radiator spectrum is scaled down by a factor of 10 to facilitate the comparison. The calculation assumes a 3.4 mm collimator located 80 m downstream of the radiator. The loss in normalized intensity with the thicker radiator, as well as the broadening of the left edge of the peak, is due

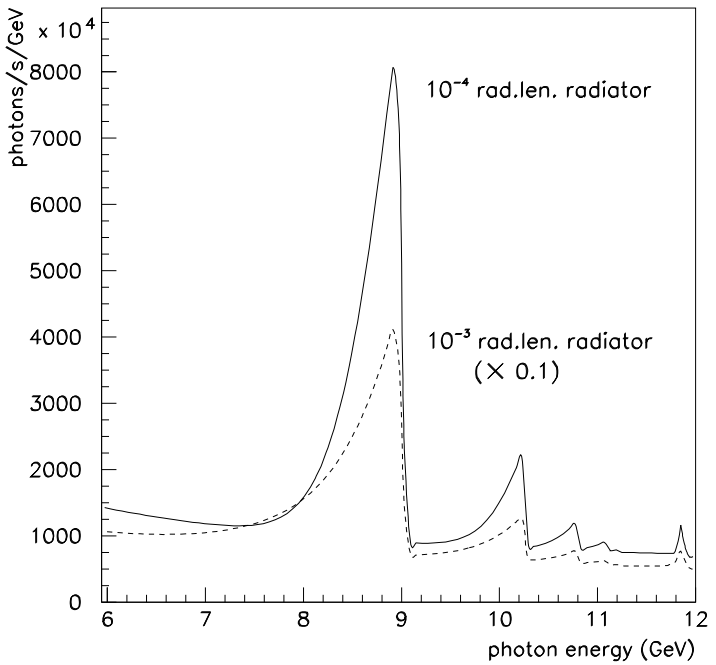

Figure 4.13: Collimated coherent bremsstrahlung spectrum from a 1μA electron beam at 12 GeV using diamond radiators of two different thicknesses. The calculation assumes a 3.4 mm collimator located 80 m from the radiator, and typical values for beam emittance and crystal quality.

to the enlarging of the photon beam spot on the collimator face from multiple scattering of the electron beam in the crystal prior to radiation. A 10^{-4} diamond radiator is 15 μm thick. The goal for GlueX is to run with crystals of thickness in the range 10 μm to 20 μm.

4.2.6 Crystal mount

It has already been shown that in order to achieve appreciable coherent gain the crystal must be oriented so that the coherent peaks appear well below the end point. Equation 4.2 then implies that the orientation must be such that the crystal momentum dotted with the beam momentum be of order m^2. Given a p of 12 GeV and q of 10 keV, this requires that the two vectors must be within 100 μr of perpendicular to each other and that, within a range of

angles of that order, the coherent peak sweeps out nearly the full range in x from 0 to 1.

Hence, to have a stable photon beam with the coherent peak positioned at the right energy, the angle between the incident electron beam and the crystal radiator must be adjustable in steps of a few μr and remain stable at this level. Since the angle of the incident beam is fixed by the beamline optics and the position of the photon collimator, all adjustments must be made by changing the orientation of the crystal. This is achieved with a precision goniometer (shown schematically in Fig. 4.14) which should provide motion on at least 5 axes. Rotation about the azimuthal axis ϕ sets the orientation of the polarization plane, rotations about the θ_v, θ_h axes set the angle of the crystal relative to the beam, and x, y translations select the position of the beam spot on the crystal. Estimates of the approximate range and step size for each of the axes are given in Table 4.2.

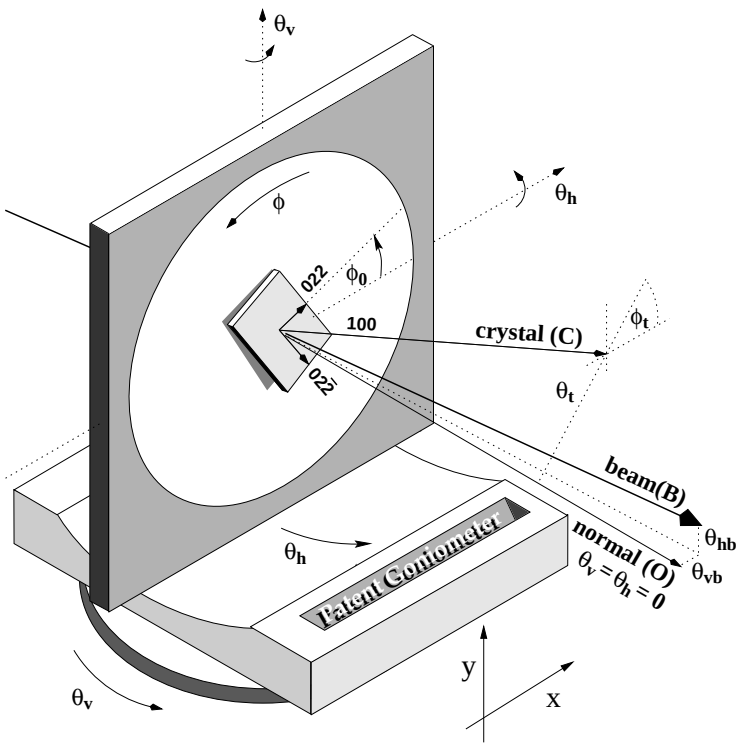

Figure 4.14: Schematic illustration of crystal mounted in goniometer

In practice several targets need to be mounted in the goniometer. The minimum requirement is a diamond crystal, an amorphous radiator, and a blank. It is also desirable to have a screen to show the position of the beam

Axis	Motion	Range	Step size
x	horizontal translation	-50 mm – +50 mm	0.01 mm
y	vertical translation	-20 mm – +20 mm	0.01 mm
θ_v	vertical rotation	-100 mr – +100 mr	10 μr
θ_h	horizontal rotation	-100 mr – +100 mr	10 μr
ϕ	azimuthal rotation	-100° – +100°	0.01°

Table 4.2: Requirements for goniometer axes

spot and a spare diamond. This means either mounting some targets off-axis on the azimuthal plate (as in the Mainz setup), or having a sixth axis to allow a target ladder to sit inside the azimuthal plate (as in the Jlab Hall B setup). A goniometer with the required precision can be obtained commercially, and would be controlled with the slow controls system.

4.2.7 Crystal alignment and monitoring

As can be seen in Fig. 4.14 the goniometer setting θ_v,θ_h defines the direction of the normal to its inner plate (O). Ideally at its zero setting $\theta_v = \theta_h = 0$ this would coincide with the electron beam direction (B), but in practice there are small offsets θ_{vb}, θ_{hb} which may vary according to the stability of the electron beam. There will also be a misalignment of the crystal lattice with respect to the inner plate due to imperfections in the mounting and in the cutting from the original stone. The 100 axis (C) will be tilted with respect to the inner plate at an angle θ_t with this maximum tilt occurring at an azimuthal angle ϕ_t. In addition, the 022 vector will be offset by ϕ_0 with respect to the horizontal. Any motion about the azimuthal axis ϕ changes the angle of the 100 axis (C) relative to the beam. The angle of the polarization plane is set by adjusting the azimuthal angle of the crystal ϕ. Hence when a new crystal is installed, the default value ϕ_0 needs to be measured. Furthermore, to position the coherent peak at the required photon energy, the angle (or *offsets*) between the beam and 100 crystal axis (C) at the chosen value of ϕ must also be established.

Feedback on the relative angle between the crystal and the beam is obtained from a photon energy spectrum derived from the tagger focal plane counters, either via scalers or a TDC hit pattern. The scaler spectrum does not show the effect of collimation (unless the scalers are gated with a downstream photon detector), but can be obtained very quickly since it does not require a triggered data acquisition system. The scaler readout is essential for the alignment

process, where the offsets are measured by carrying out a series of scans in which 2d histograms of photon energy vs. crystal angle are built up by moving the goniometer in a sequence of small angular steps and reading the tagger scalers. In addition to providing the feedback required for alignment, the focal plane counters provide essential online diagnostics to monitor drifts in angles caused by the beam tuning, or thermal effects in the crystal mount. If necessary a feedback system could be implemented via the slow control system, where any drift in the position of the coherent peak could be corrected by periodically adjusting the goniometer within predefined limits.

The spectrum obtained from the tagger focal plane can also provide online monitoring of the photon polarization to within 5% by fitting with an analytic bremsstrahlung code. A more detailed discussion of polarimetry appears in the following sections.

4.2.8 Crystal lifetime

The best information regarding crystal degradation comes from X-ray studies performed by the Glasgow group of a diamond which had been used in the MAMI coherent bremsstrahlung source at Mainz for several years. The electron beam on the Mainz crystal had a diameter of about 100 μm and it was estimated that around 10^{20} electrons had passed through the diamond during its use in the source. There was a small greenish black spot where the beam had hit the diamond.

The X-ray rocking curve measurements showed that considerable damage had occurred to the integrity of the crystal structure in the center of the beam spot. However 2 mm away from the damage center the width of the diffraction peak was the same as it had been for the pristine crystal, which indicates that the lifetime of the crystal could be extended by occasionally moving the beam spot on the face of the crystal.

The area of the MAMI beam spot on the radiator is two orders of magnitude smaller than what is being planned for GlueX in Hall D. A larger spot means a longer crystal lifetime before radiation damage substantially degrades its crystal properties. Appropriately scaled, the exposure of the Mainz crystal would correspond to 15 years of running in Hall D at the full intensity of 3 μA without a spot move. Plans for the Hall D source are to keep the exposure about three orders of magnitude less than this. At the SLAC coherent bremsstrahlung beam line it was found that the performance of their diamond radiators had degraded noticeably after a total charge of 3 Coulombs had been accumulated over a spot of size roughly 2 mm r.m.s., leading to a limit of about 0.25 Coulomb/ mm^2 [7]. Taking this as a conservative estimate

for the allowed exposure, the source can run at a full intensity of 3 μA for 60 hours before it is necessary to move the spot on the crystal. If it had no bad zones, a square crystal of 5×5 mm^2 would accommodate 5 spot moves before the crystal would need to be replaced. SLAC researchers were able to recover a good performance for the damaged crystals by putting them through an annealing process. Further research and development will be required to determine whether crystal recovery through annealing is an effective way to reduce the operating costs of the HALL D source.

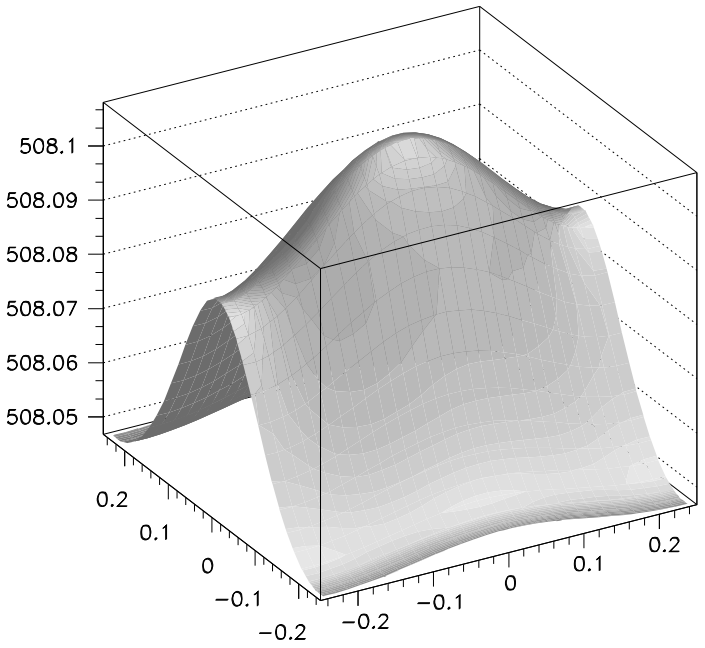

Figure 4.15: Calculated temperature profile of diamond crystal with a 12 GeV beam at 3 μA. The crystal dimensions are 5 mm $\times 5$ mm $\times 15$ μm. The ambient room temperature was taken to be 27^o C (300 K). The x-y asymmetry is caused by the elliptical shape of the electron beam spot on the radiator.

Another issue related to crystal degradation is that of heat dissipation for very thin crystals. The heat comes from the ionization energy loss of the beam as it passes through the crystal. Although this is small compared to the bremsstrahlung energy loss, it is not entirely negligible at these beam currents. It can be calculated using the restricted energy loss formula, which

yields 21 mW for a 15 μm (10^{-4} radiation lengths) crystal at a current of 3 μA. This is not much power, but the crystal is very thin. Heat dissipation is through radiation and conduction. Diamond has a very high melting point; at low pressures it sublimates at about 4027^o C. However at normal pressures it begins to transform into graphite above 707^o C, at a rate that depends on temperature. It is therefore important that the crystal at the center of the beam spot stay well below this limit.

The diffusion equation including a heating term and one for radiative cooling can be written as

$$\rho C_P \, a \, \frac{dT}{dt} = h(x,y) - 2\sigma\epsilon \left(T^4 - T_0^4\right) + \kappa \, a \nabla^2 T$$

where the heating term $h(x,y)$ has units of power/area, σ is the Stefan-Boltzmann constant, ϵ is the emissivity of diamond, rho is the density, C_P is the heat capacity, κ is the coefficient of thermal conduction, and a is the thickness of the crystal. T_0 is the ambient temperature of the environment and T is the local crystal temperature, a function of space and time coordinates. After a certain time, T converges to the steady-state solution shown in Fig. 4.15. The calculation used a crystal of dimensions 5×5 mm^2 and a beam current of 3 μA. The conductivity of diamond is sufficient to prevent significant temperature gradients across the crystal even for very thin wafers, and radiative cooling alone is sufficient to dissipate the heat being generated by the beam passing through the crystal so that the crystal mount does not need to act as a heat sink. The time constant for warm-up and cool-down is approximately 10 s.

4.3 Electron beam

The performance of the photon source is dependent upon the parameters of the electron beam in several important areas. These parameters are listed in Table 4.3. The first column of numbers gives the set of parameters that have been adopted as the design goals for the source. These are the values that have been taken as input in calculating the characteristics of the coherent bremsstrahlung source. The second column of numbers was obtained from a concrete design of the Hall D beam line [8] that was carried out by members of the Jefferson Lab Accelerator Division. The exact choice of the final parameters has not yet been made, but the preliminary design shows that all of the design goals can be met within the available real estate. The reduction of the radiator-collimator distance from 80 to 75 m does not significantly affect the performance of the source.

parameter	design goals	design results
energy	12 GeV	12 GeV
electron polarization	not required	available
minimum useful current	100 pA	100 pA
maximum useful current	3 μA	5 μA
r.m.s. energy spread	< 10 MeV	7 MeV
transverse x emittance	10 $mm{\cdot}\mu$r	10 $mm{\cdot}\mu$r
transverse y emittance	2.5 $mm{\cdot}\mu$r	2.3 $mm{\cdot}\mu$r
x-dispersion at radiator	none	negligible
y-dispersion at radiator	none	< 1 cm
x spot size at radiator	1.7 mm r.m.s.	1.55 mm r.m.s.
y spot size at radiator	0.7 mm r.m.s.	0.55 mm r.m.s.
x image size at collimator	0.5 mm r.m.s.	0.54 mm r.m.s.
y image size at collimator	0.5 mm r.m.s.	0.52 mm r.m.s.
distance radiator to collimator	80 m	75 m
position stability	± 200 μm	

Table 4.3: Electron beam properties that were asked for (column 2) and obtained (column 3) in a preliminary optics design for the transport line connecting the accelerator to the Hall D photon source.

The following sections highlight the particular properties of the electron beam which have a special impact on the performance of the source.

4.3.1 Beam polarization

It has already been stated that to generate bremsstrahlung photons with linear polarization it is necessary to use an oriented crystal radiator. However photons with circular polarization are produced by ordinary incoherent bremsstrahlung any time the incident electrons are longitudinally polarized. In fact for 9 GeV photons produced by 12 GeV electrons, the transfer from electron beam longitudinal polarization to photon beam circular polarization is greater than 80%. This raises the question of what happens when one has longitudinally-polarized electrons incident on an oriented crystal radiator. What happens in this case is that the photon beam is elliptically polarized; it carries both circular and linear polarization. There is a sum rule that limits the sum of the squares of the linear plus circular polarizations to be no greater than 1. Hence one sees the linear polarization in coherent bremsstrahlung going to zero as one approaches the end-point energy (see Fig. 4.8) while at the same time the circular polarization goes to 1 at the end-point (assuming electrons of 100% longitudinal polarization).

The statement in Table 4.3 that electron beam polarization is not required for the GlueX experiment in Hall D is correct, but it is not correct to assume that the photon source is independent of the state of polarization of the electron beam. The presence of a non-zero circular polarization in the Hall D photon beam will, in principle, produce observable effects in the angular distributions measured in photoproduction reactions. This means that there will be an important coupling between the GlueX program and the other experimental halls whose programs sometimes require them to have control over the beam polarization. This coupling can be eliminated by setting up the tune of the electron beam line to Hall D such that the longitudinal component of the electron beam polarization is rotated to zero at the crystal radiator. Whether the decision is made to rotate it away or simply to measure its value periodically, this consideration underlines the importance of having a means to measure photon beam polarization in a way that does not rely on *a priori* knowledge of the properties of the electron beam.

Although the ability of the source to produce photon beams with both circular and linear polarization complicates operation when one of them is desired without the other, it does increase the versatility of the source. The two kinds of polarization are controlled independently of one other, and together they give access to a more complete set of polarization observables than would

be possible with only one or the other.

4.3.2 Beam emittance

The values for the electron beam emittances shown in Table 4.3 are estimates based upon the parameters of the current machine projected to 12 GeV[8]. The definition of emittance used here is the product of the r.m.s. widths of the beam in transverse position and divergence angle. Because synchrotron radiation inside the accelerator occurs mainly in the horizontal plane, the emittance values in x are generally larger than those for y. The two vertical bends required for bringing the 12 GeV beam from the level of the accelerator up to beam height in HALL D do increase the vertical emittance a small amount over its value inside the machine; this effect has been included in computing the vertical emittance shown in Table 4.3.

The longitudinal emittance of the beam is important as it is the limiting factor in determining the ultimate energy resolution of the tagger. The design goal of 0.1% photon energy resolution is well matched to the energy spread expected for the CEBAF beam at 12 GeV.

The place where transverse emittance plays a critical role is at the photon collimator. For optimum effectiveness in collimation it is important that the virtual electron beam spot at the collimator position be as small as possible. The electron beam does not actually reach the photon collimator, being bent into the dump by the tagger magnet shortly after the radiator. But considering the optics of the electron beam as if the tagger dipole were switched off, the electron beam at the radiator can be projected forward to form a virtual image on the collimator entrance plane. The position and size of this virtual spot determines the definition of 0° emission angle for the photons. If this spot is small compared to the collimator aperture and is correctly centered then the bremsstrahlung photons of a given emission angle α intersect the entrance plane of the collimator in a well-defined ring of radius $D\alpha$ concentric with the collimator aperture, where D is the distance between the radiator and the collimator entrance plane. In this way a collimator of diameter d passes only those photons of emission angle $\alpha \leq d/2D$. If however the size of the virtual spot is comparable to or larger than the collimator aperture then the ring image of photons of a given emission angle α is smeared out, so that the effect of collimation is simply to reduce the intensity of the beam but not to enhance the coherent component.

Note that this analysis does not place any specific limits on the size of the beam at the radiator. The beam spot can and should be larger there to increase the lifetime of the crystal between spot moves. For the SLAC

coherent bremsstrahlung source the beam spot at the radiator was about 2 *mm* r.m.s., focused down to a 1 *mm* r.m.s. virtual spot at the primary collimator positioned 91 *m* downstream of the radiator.

The superior emittance characteristics of the CEBAF beam allow the transverse dimensions to be somewhat smaller than this for the HALL D source, more so in the vertical than the horizontal dimension. The difference between the horizontal and vertical emittance of the CEBAF beam implies that making the spot round at the radiator implies an elliptical virtual spot at the collimator, and *vice versa*. It is difficult to construct a collimator with an elliptical aperture, so the choice was made to make the virtual spot round. This is why the beam spot on the radiator is asymmetric.

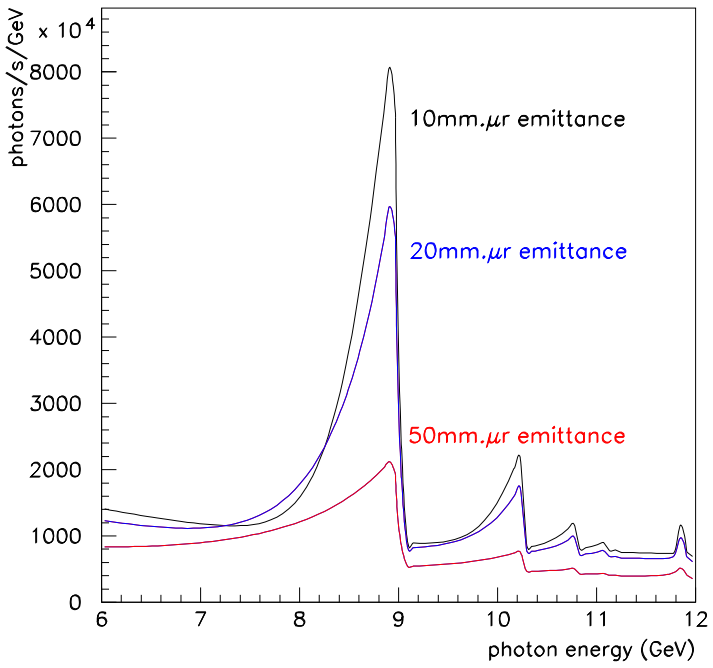

Figure 4.16: Coherent photon spectrum for three different values of the electron beam transverse emittance. The horizontal (shown on the plot) and vertical emittances are assumed to scale together. A 3.4 *mm* collimator located 80 *m* from the radiator was used for this calculation.

Figure 4.16 shows how the collimated photon spectrum depends upon the transverse emittance of the electron beam. To generate this plot the increases

in emittance were simply translated into an increased virtual spot size on the collimator. This was done because it was assumed that the spot size of the electron beam on the radiator, already close to 2 mm r.m.s., cannot be further inflated and stay contained within the limits of the crystal. When the virtual spot size becomes comparable with the collimator aperture then the collimation is rendered ineffective, and the photon spectrum and polarization revert to their uncollimated values. There is another connection between focal spot size and beam emittance that is connected with the requirement that all electrons enter the radiator at the same incidence angle with respect to the planes of the crystal. Practically, the divergence does not broaden the coherent peak provided that it is kept below the mosaic spread of the crystal. A conservative value for the allowable angular divergence δ in the electron beam at the radiator would then be 20 μr . Taken together with a 500 μm r.m.s. spot size at the focus, this leads to an emittance of 10 $mm{\cdot}\mu r$ at 12 GeV. This corresponds to the upper curve in Fig. 4.16.

4.3.3 Electron beam line optics

Translating the beam emittance into r.m.s. values for the beam radius and divergence requires the knowledge of the β function of the transport line between the accelerator and the radiator, defined as the ratio of the beam size to its angular divergence.

The preliminary optics design [8] of the Hall D beam line (see Table 4.3) is shown in Fig. 4.17. The horizontal and vertical beta functions are shown in the upper and lower panels, respectively. Between the two panels is shown a schematic of the transport lattice. The design begins at the exit of the beam from the end of the linac and ends at Hall D. The z coordinate is measured along the axis of the linac, with its origin at the mid-point of the accelerator. Fig. 4.18 shows the beta functions translated into r.m.s. beam size and shifted to place the radiator at the origin. The design allows the ratio of the spot sizes at the radiator and collimator to be adjusted over about an order of magnitude simply by changing the current in the beam line elements. In this way it will be possible to optimize the optics for a given size of crystal and collimator after beams are delivered to the hall, and more precise values for the emittances are in hand.

Not only must the virtual electron spot be small enough to fit within the collimator aperture, but it must also be centered on the aperture and stable. In order to maintain a stable beam position on the collimator, the SLAC experiment [2] instrumented the collimator with a secondary-emission detector. The detector was of the “pin-cushion” design and was installed between

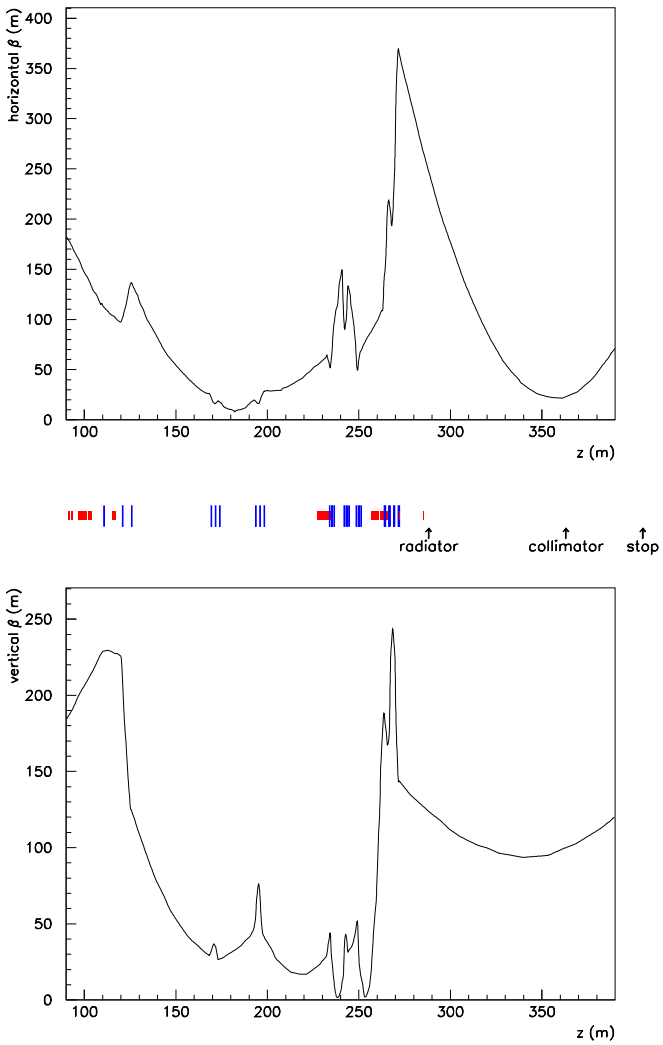

Figure 4.17: Horizontal (upper panel) and vertical (lower panel) beta functions from the preliminary optics design for the transport line from the accelerator to the HALL D photon source. The beam line lattice is shown schematically between the two panels, with dipole magnets represented by the short boxes and quadrupoles by the taller lines. The z coordinate is equal to the flight path length of the electrons starting at the center of the linac, up to an error of a few cm from the vertical motion of the beam.

segments of the collimator near the position of the shower maximum. The readout was divided into four quadrants, which read equal currents when the beam was properly aligned on the collimator. The readout was connected via

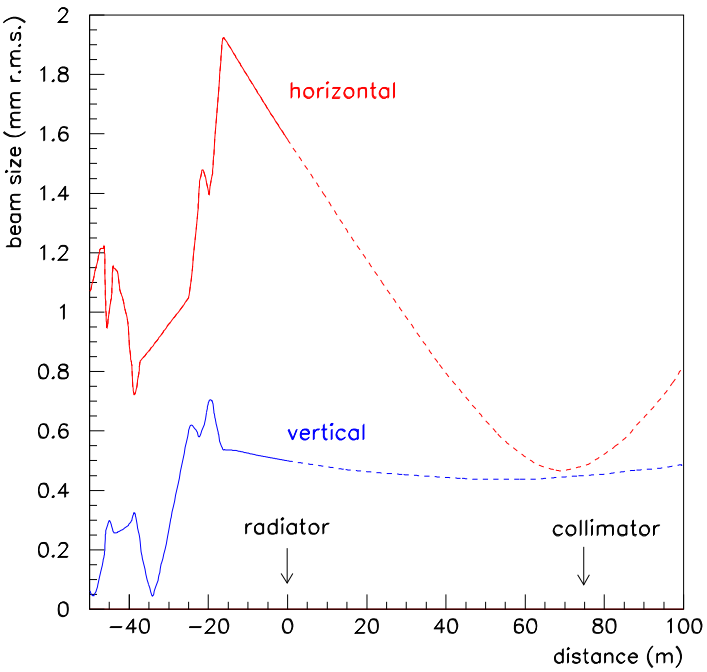

Figure 4.18: Horizontal and vertical r.m.s. envelopes for the electron beam in the region of the photon source, as derived from the beam emittance and beta functions of Fig. 4.17. The origin of the z coordinate has been placed at the radiator. In the region between the radiator and the collimator the envelope refers to the projected image of the electron beam, and does not describe the size of a physical beam that exists in that region.

a feedback loop to the last steering elements on the electron beam line prior to the radiator. Over that distance a bend of only 10 μr results in a shift of 1 mm at the collimator position. The small deflections that are necessary to keep the beam centered on the collimator do not produce appreciable walk in the beam-crystal angle. This means that an active feedback system can be set up between the instrumented collimator and deflection coils just upstream of the radiator, that can operate independent of the crystal alignment system to keep the electron beam aimed at the center of the collimator.

The experimental program in parity violation at Jefferson Lab has already demonstrated a position stabilization circuit that is able to keep the beam position steady to within 20 μm over a 20 m lever arm. A less sophisticated

version of this circuit will meet the position stability requirements for the HALL D photon source.

4.3.4 Electron beam dump

The electron beam is dumped in the horizontal plane, as shown in figure 4.4. The horizontal bend offers several advantages over dumping the beam into the ground. The tagger magnet is easier to support if it sits in the horizontal position. It is also easier to mount and service the focal plane instrumentation in this position. The dump itself is also more accessible in case it needs to be serviced. An above-ground dump also affords the possibility of running parasitic beam dump experiments that do not interfere with the operation of the experimental hall.

The primary design requirement for the electron beam dump is that it has a sufficiently high capacity to handle beams of the highest intensities foreseen for the GLUEX experiment in HALL D. A 60 kW design would provide a a healthy margin for operation of a 12 GeV beam at 3 μA and sufficient capacity to handle 3 μA at 20 GeV in the case of a further upgrade.

4.3.5 Beam containment and shielding

There are three factors that must be taken into account in the design of the shielding for the HALL D beam line. The first is the constraint on the background radiation level that is allowed outside the beam enclosure. The second factor is the level of radiation in the experimental hall which can generate background in the detector during normal running. The third factor is the control of hazards which may occur in the event of a failure of one or more of the beam delivery systems. The first issue has been studied by the Jefferson Laboratory Radiation Controls Group, and will be discussed further in the chapter on Civil Construction. The latter two considerations have been studied by a working group headed by L. Keller (SLAC). A summary of their recommendations [9] follows.

Assuming that the electron beam dump is shielded to the requirements of radiation safety, the next source of background radiation in the experimental hall is the photon collimator. The most penetrating forms of radiation from the collimator are muons and neutrons. A Monte Carlo simulation, assuming a 13 radiation lengths tungsten collimator followed by a sweeping magnet and 5 m of iron shielding, predicted a flux of 1.4×10^3 $\mu^{\pm}$/s incident on the detector at full operating beam intensity. This is a negligible rate compared with the trigger rate from photon interactions in the target. The flux of

neutrons from the collimator is more difficult to calculate, but some fraction of 1 m of concrete shielding will be needed surrounding the collimator enclosure to shield the hall from energetic neutrons.

With regard to hazards associated with the accidental failure of beam line elements or controls, the following measures were recommended in the Keller study [9] and have been incorporated into the HALL D design. The dipole string that bends the electron beam up towards the surface from the below ground and then bends it back horizontal will be connected in series so that failure of a magnet supply or current control electronics cannot result in the beam being steered into the ceiling of the tagger building. The power supply feeding this string of magnets will be protected by a meter relay that shuts off if the current varies from its desired value outside a predefined tolerance. A similar meter relay will also be used on the power supply of the tagger magnet. An electron beam collimator with a burn-through monitor will be located just upstream of the radiator to prevent a mis-steered beam from using radiator support structures as a bremsstrahlung target. Permanent magnets will be located in the upstream region of the photon beam line to bend an errant electron beam into the ground in the case that beam is present while the tagger magnet is off. An emergency beam stop will be installed in the bottom of the photon beam line to catch the errant beam deflected by the permanent magnets. It will be equipped with a current monitor to shut down the primary beam any time electrons are sensed in the photon beam line. Ion chambers located upstream of the photon collimator, and also at the entrance to the photon beam dump behind the experiment, will monitor the total flux in the photon beam and shut off the beam if the flux exceeds a safe value.

4.4 Tagging spectrometer

4.4.1 Specifications

To satisfy the needs of the GLUEX physics program, the tagged photon spectrometer should meet the following specifications:

1. Photon energy detection from 70% to 75% of E_0 with energy resolution of about 0.1% r.m.s. Percentages refer to the primary beam energy E_0, i.e. "0.1%" means 12 MeV energy resolution for a 12 GeV beam.

2. A detector system which allows a counting rate of at least 5×10^6 electrons per second per 0.1% over this range of photon energies.

3. An additional capability for photon energy detection from 25% to 90% of E_0, with less stringent resolution and count rate requirements .

4. A quadrupole magnet between the radiator and dipole spectrometer which images the beam spot on the radiator onto a line on the focal plane. This feature makes it possible to envision the use of focal plane counters with two-dimensional readout, with which one could enhance the tagging efficiency of the source. Focal plane detectors with two-dimensional readout are considered as a possible upgrade beyond the baseline design presented in this chapter. Any improvements obtained using this technique would be over and above the performance figures presented in this report.

The system described below, based on a room-temperature design, meets all of these criteria. The option of a superconducting design was also studied. With a superconducting magnet, the spectrometer could operate at much higher fields, offering the possibility of some space savings in the size of the tagger focal plane array and larger head-room for future possible energy upgrades beyond 12 GeV. An iron yoke design was found which would clamp the 5 T field sufficiently to make it possible to operate normal phototubes on the nearby tagger focal plane. However, as shown below, rate considerations require a degree of segmentation in the tagging counters such that it is impractical to increase the dispersion along the focal plane above what is provided by a 1.5 T room temperature magnet. That being the case, it was decided that considerations of upgrade margin and electrical power alone do not justify the additional cost and complexity of a superconducting magnet.

4.4.2 Magnet

The original design of the tagger spectrometer, which incorporated a single, long dipole magnet $\sim$ 6.1 m in length weighing about 100 tons, has been changed to replace the single dipole with a configuration consisting of two identical dipoles in series with each other.

The main reasons for this change are:

1. It will be difficult to find a supplier of $\sim$ 6.5 m lengths of high quality magnetic iron at a reasonable cost.

2. Since the weight of the top and bottom yoke pieces for a single dipole tagger will weigh more that 20 tons, either a crane with a capacity of

more than 20 tons or heavy duty lifting equipment will be necessary to install the magnet or undertake any future repairs or modifications.

3. The long structure of a single dipole tagger will be difficult to install.

4. Since the energy degraded bremsstrahlung electrons exit a tagger along the whole of its length, it is necessary to have the exit completely open. Due to the attractive magnetic force between the poles, the aperture along the exit will distort when the field is present. The effect of this distortion will probably be less for two smaller dipoles than for a single long dipole.

5. The smaller magnets can be made by more manufacturers and will probably be cheaper.

6. Building costs will be less for the two dipole option - cheaper crane, smaller access doors etc.

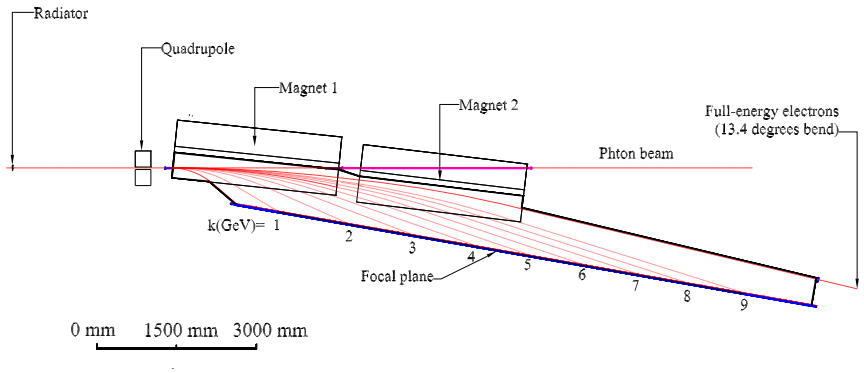

Figure 4.19: A plan view of the tagging spectrometer from above, showing the path of the primary beam and the trajectory of post-bremsstrahlung electrons of various recoil momenta.

The parameters of the two dipole tagger are shown in Table 4.4. The object distance is listed explicitly since it has been increased from 1.5 m to 3.0 m. This improves the resolution by around 30% and gives more room for the goniometer vacuum chamber, the quadrupole and monitoring devices. A plan view of the layout of the spectrometer is shown in Figure 4.19.

The coils for the two dipole tagger will be run in series from a single power supply.

Radius of curvature	26.7 m
Full-energy deflection	13.4^{O}
Object distance	3 m
Field at 12 GeV	1.5 Tesla
Gap width	3.0 cm
Length of each pole	3.1 m
Weight of each dipole	38 tons
Length of focal plane (25% to 90% of E_0)	$\sim$ 9.0 m
Coil power	30 kW

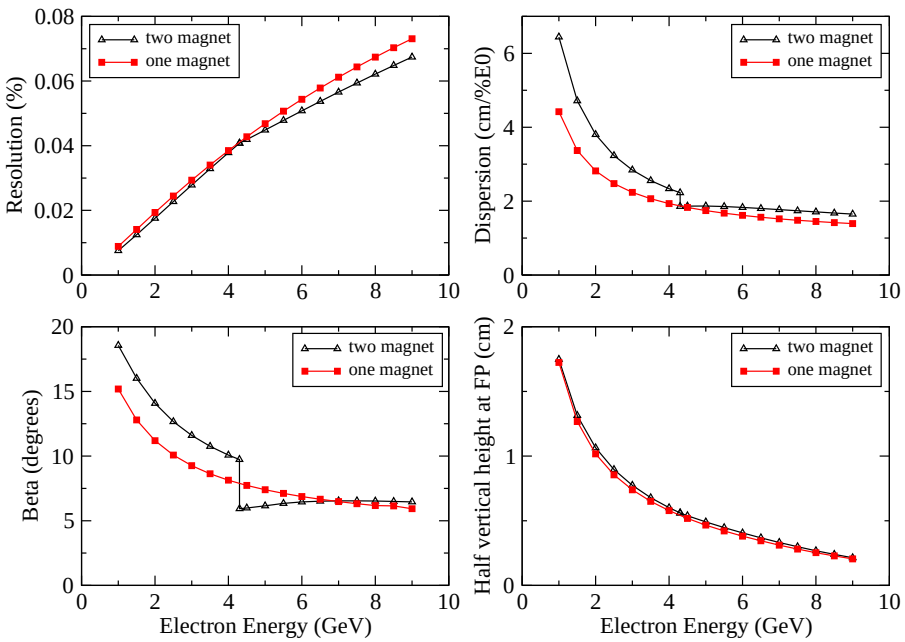

Figure 4.20: Comparison of optics properties between the one dipole and the two dipole tagger.

The first dipole magnet analyzes electrons from 1 to 4.3 GeVcorresponding to photon energies of 7.7 to 11 GeV, and the second magnet analysis electrons from 4.3 9 GeV, corresponding to photon energies of 3 to 7.7 GeV. This is ideally matched to GlueX which requires photons in the energy range covered by the first dipole. It is also clear that a two dipole magnet system is optimum, since with more magnets, the energy range required by GlueX would probably have to be shared between different dipoles.

The pole gap has been increased from 2.0 to 3.0 cm. The larger gap is more accessible, and is less susceptible to any changes to the pole gap caused by the magnetic field. Furthermore since only $\sim 30\,kW$ are required for the 3.0 cm gap -compared to $\sim 17.6\,kW$ for the 2.0 cm gap - the coil power consumption remains modest.

The two dipole magnet configuration was only adopted after extensive investigations into the magnetic optics confirmed it is possible to design such a system with a continuous focal plane. First order TRANSPORT calculations of the dispersion, resolution and vertical height along the focal plane, as well as beta, [illegible] e, are compare

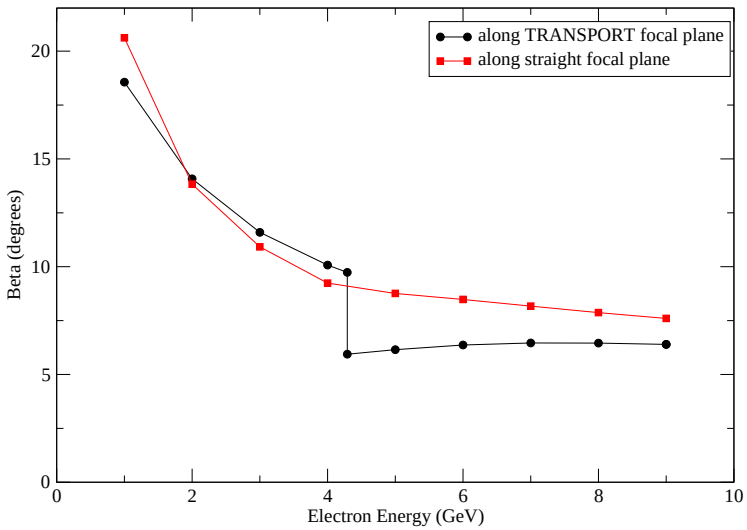

Figure 4.21: Comparison between the beta for the focal plane calculated using TRANSPORT and the beta for the straight focal plane determined according to the TOSCA results.

The resolution and vertical height are essentially unaltered. Although the dispersion shows a small discontinuity at an electron energy $\sim 4.3\,GeV$, which is where the focal planes from the dipoles join, along the whole extent of the focal plane the dispersion from the two dipole tagger is slightly larger. However, beta shows a significant discontinuity at the join of the focal planes. This apparent effect was examined in more detail by ray tracing electron trajectories through a 3-D magnetic field obtained from TOSCA. The ray tracing calculations were also used to find an acceptable location for a straight focal plane which is displaced slightly from the curved TRANSPORT focal plane. Figure 4.21 compares the variation of beta along the straight focal plane ob-

tained using TOSCA, and along the first order TRANSPORT focal plane. It shows that the realistic field computed by TOSCA leads to a smooth variation for beta and also shows that beta is larger for the higher energy section of the focal plane. The magnetic optics parameters, calculated by TRANSPORT along the straight focal plane, are shown in section 4.4.3.

Several designs have been considered for the vacuum system. The most promising approach is to use the magnet poles as part of the vacuum chamber. Either the poles could be welded to a stainless steel vacuum chamber, or the seals between the vacuum chamber and the poles could be made by compressing a viton O-ring between the top and bottom lids of the vacuum chamber and a lip machined round the pole shoes.

A reasonably detailed design for a two dipole magnet tagger, which incorporates a vacuum chamber using O-ring seals, has been completed. The design has been sent to Russian groups within the GlueX collaboration who will examine the technical feasibility of the design and investigate if ISTC funding can be obtained to construct the tagging spectrometer. It should be possible to assemble and test the complete spectrometer in Russia since a feature of the design which uses O-ring seals is that the spectrometer can be fully assembled and tested in the factory where it is built, and then be taken apart and subsequently re-assembled in Jefferson Lab.

The detector package is divided into two parts: a set of 141 fixed scintillation counters spanning the full energy range from 25% to 95%, and a movable "microscope" of more finely-segmented counters designed to span the region of the coherent peak.

The fixed array provides access to the full tagged photon spectrum, albeit at a modest energy resolution of 0.5% and reduced photon spectral intensity. These detectors are well suited for running with a broadband incoherent bremsstrahlung source. They enable experiments to be performed with the highest photon energies possible with the source. When running with a coherent source they play an essential role in the crystal alignment procedure, and provide a continuous monitor of the performance of the source. The microscope is needed in order to run the source in coherent mode at the highest polarization and intensities, and whenever energy resolution better than 0.5% is required. Using the microscope, the source is capable of producing photon spectral intensities in excess of 2×10^8 photons/GeV, although accidental tagging rates will limit normal operation to somewhat less than this.

k (GeV)	Bend (deg)	Drift (m)	Angle (deg)	cm/%E_0 perp.to ray	cm/%E_0 along FP
6	17.270	3.7790	6.035	1.467	13.956
7	17.664	3.2039	6.428	1.568	14.008
8	18.28	2.6276	6.992	1.716	14.096
9	19.108	2.0485	7.872	1.954	14.264
10	20.695	1.4626	9.459	2.407	14.644
11	24.608	0.8560	13.372	3.668	15.860

Table 4.5: Geometrical parameters of the tagging spectrometer for $E_0 = 12\ GeV$: Bend = deflection angle; Drift = distance from exit edge to focal plane; Angle = angle between electron path and focal plane; $cm/\%E_0$ = dispersion in units of cm per percent of the incident energy

4.4.3 Spectrometer Optics

Table 4.5 and Table 4.6 give some of the tagger optics parameters as functions of the photon energy. They were calculated for the one-magnet spectrometer option, but the differences between the optics of the two-magnet and one-magnet designs are not very significant, as shown in Figs. 4.20-4.21. The energy resolution and transverse position resolution were calculated assuming the beam properties listed in Table 4.3. The intrinsic energy resolution (i.e. the energy resolution independent of detector size) is limited in most cases by the 0.08% energy spread of the primary electron beam.

At the focal plane, the characteristic bremsstrahlung angle corresponds to a few millimeters of transverse displacement. The vertical beam spot size at the radiator (0.5 mm r.m.s.) contributes a comparable amount because of the large transverse magnification in the dipole transport matrix. However, placing a quadrupole magnet between the radiator and the tagger dipole magnet reduces this magnification nearly to zero over a substantial range of photon energies without substantially changing the other optical properties. Including the quadrupole in the design makes possible a future upgrade of the photon source to employ tagging detectors with two-dimensional readout.

k (GeV)	(x x) (mm/mm)	(y y) (mm/mm)	(y y') (mm/mr)	Δk_{beam} ($\%E_0$)	Δk_{spot} ($\%E_0$)	Δk_{tot} ($\%E_0$)	Δy_{tot} (mm)	y_{char} (mm)
Without quadrupole:								
6	-0.701	2.737	18.882	0.080	0.081	0.114	1.372	0.804
7	-0.667	2.708	16.538	0.080	0.072	0.108	1.357	0.986
8	-0.625	2.670	14.178	0.080	0.062	0.101	1.337	1.207
9	-0.569	2.617	11.788	0.080	0.050	0.094	1.310	1.506
10	-0.494	2.539	9.341	0.080	0.035	0.087	1.270	1.989
11	-0.389	2.402	6.745	0.080	0.018	0.082	1.201	3.159
With quadrupole: (length = 50 cm, gradient = -0.4 kGauss/cm)								
6	-0.628	0.451	17.622	0.080	0.073	0.108	0.242	0.750
7	-0.583	0.348	15.121	0.080	0.063	0.102	0.190	0.901
8	-0.526	0.202	12.535	0.080	0.052	0.095	0.119	1.068
9	-0.449	-0.024	9.792	0.080	0.039	0.089	0.050	1.251
10	-0.338	-0.427	6.699	0.080	0.024	0.083	0.216	1.426
11	-0.162	-0.416	2.474	0.080	0.008	0.080	0.708	1.159

Table 4.6: Optical properties and resolutions of the tagging spectrometer at the focal plane, for $E_0 = 12\ GeV$: (x x),(y y),(y y') = first-order transport matrix elements where x and y are radial and transverse coordinates respectively; the focal plane is defined by (x x')=0.; Δk_{beam} = r.m.s. energy resolution due to beam energy uncertainty; Δk_{spot} = r.m.s. energy resolution due to spot size on radiator; Δk_{tot} = total r.m.s. energy resolution excluding detector size; Δy_{tot} = transverse r.m.s. position resolution due to spot size on radiator; y_{char} = transverse size corresponding to one characteristic electron angle $\theta_{Ce} = (m/E_0)(k/(E_0 - k))$.

4.4.4 Tagger detectors

Fixed focal plane array

Tagging of photons over the full range from 25% to 95% of E_0 is not required as part of the physics program here proposed for GlueX, but is desirable for two separate reasons. First, it will increase the flexibility of the source by providing a broad-band incoherent bremsstrahlung tagging mode, enabling access to photons of the highest energy possible at Jefferson Lab. Second, the process of aligning the crystal radiator for coherent bremsstrahlung requires rotation about several axes and rapid observation of the resulting energy spectra, as described in section 4.2.7. The low-energy portion of the spectrum, between about 25% and 50% of E_0, is most sensitive to these rotations, and experience with the coherent bremsstrahlung beam at Mainz [11, 12] indicates that the alignment process would be severely compromised if photon energies below 0.5 E_0 were not measurable.

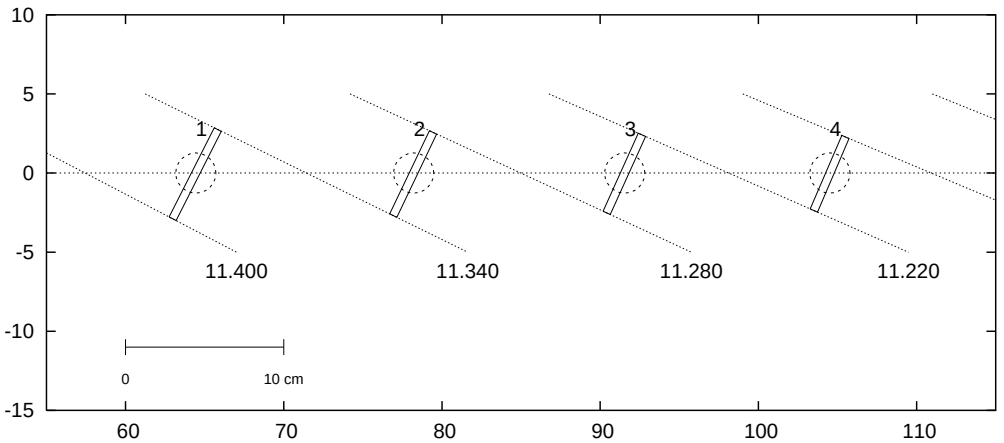

Figure 4.22: Layout of the tagging counters on the high-energy end of the tagger focal plane, corresponding to the lowest-energy electrons from the spectrometer. The view is from above.

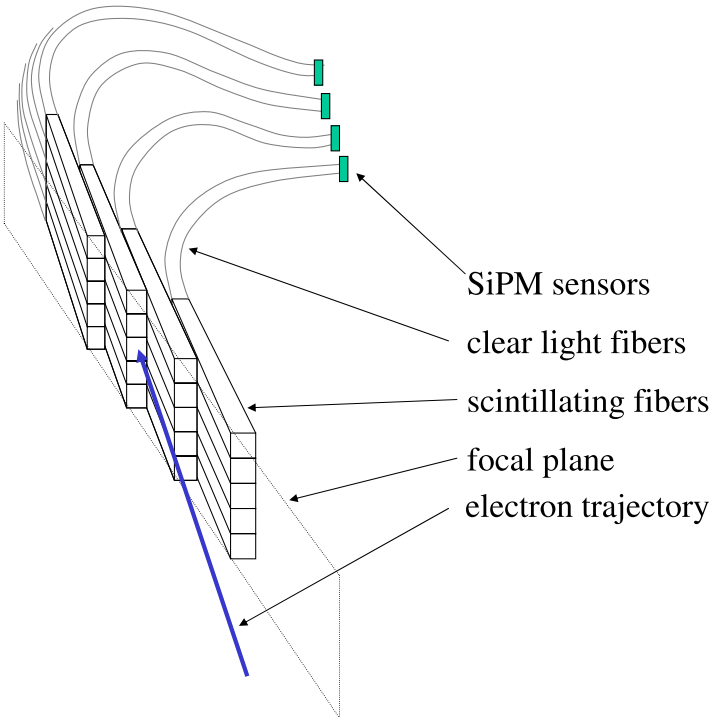

Figure 4.23: Conceptual design of a segment of the tagger microscope, showing the two-dimensional array of scintillating fibers and the clear fiber light guides that couple the light to the silicon photomultipliers.

The design for the fixed tagger focal plane array consists of 141 non-overlapping scintillation counters. The scintillators are 0.5 cm thick and 4 cm high and are read out by 1-inch phototubes located below the mid-plane of the spectrometer. The scintillator paddles are oriented perpendicular to the scattered electron rays and are distributed along the focal plane to give essentially 100% coverage of the range from 25% to 95% of E_0. The size and spacing of the counters varies along the focal plane, according to the dispersion and crossing angle listed in Table 4.5. The high-energy end of the array is shown in Fig. 4.22, which corresponds to the lowest-energy electrons from the spectrometer.

Focal plane microscope detectors

The design energy resolution of 0.1% r.m.s. (see Table 4.6) is met by non-overlapping detectors which span an energy range of 0.1% each. The principal limitation on detector size is imposed by the design goal of tagging collimated photons at rates up to 100 MHz over the coherent peak. The nominal collimated coherent peak has its highest intensity between about 8.5 and 9 GeV (see Fig. 4.6). However, the the tagger sees both collimated and uncollimated photons, and the total tagging rate in this region is more than twice the collimated rate (see Fig. 4.6), about 250 MHz. The nominal position of the microscope on the focal plane is spanning the region 70% - 75% of E_0. Dividing this range into 80 bins of equal size limits all channels to less than 5 MHz, which is well within the operating range of the silicon photomultiplier (SiPM) devices foreseen to be used for this detector.

The detector is composed of a two-dimensional array of square scintillating fibers of cross section 1 mm^2, as shown in Fig. 4.23. Electrons from the spectrometer follow a path approximately parallel to the axis of the fibers, creating a large light yield which effectively suppresses omnidirectional background in the hall and permits the operation of the SiPM detectors with a high discriminator threshold where their dark rate is low. Multiple scattering of electrons in the fiber material effectively produces some degree of overlap between the channels, but does not appreciably degrade the energy resolution of the device. Clear fibers attached to the back end of the scintillating fibers transport the light out of the spectrometer mid-plane to a region with low radiation where the SiPM detectors are located, each with an active area of 1 mm^2. The microscope will be located immediately in front of the fixed array.

In the baseline operating mode, all five fibers in a column shown in Fig. 4.23 will be summed into one electronics channel. The vertical segmentation of the device also permits its operation in an enhanced mode, where only one fiber in each column is active. In the enhanced mode with the tagger quadrupole switched on, the detector counts only a narrow band of scattered electrons that lies close to the spectrometer mid-plane. This has the advantage that the tagger is blind to those electrons which scatter at large vertical angles in the radiator, whose corresponding photon will be lost on the photon collimator. This can be accomplished efficiently by delivering the power to the SiPM devices independently by row. Simply by selectively powering the individual rows of the array, the readout can be switched from tagging the full vertical range of the beam to counting only a central stripe which corresponds to the size of the photon collimator.

4.4.5 Beam dump optics

Although the full-energy beam leaving the tagger magnet is diverging in both directions, the range of angles is small enough that the beam does not blow up rapidly. For a dump distance of 30 m the r.m.s. beam size is 6.3 mm horizontal (dominated by the 0.08% beam energy spread) and 0.7 mm vertical (combination of vertical spot size and multiple scattering in a 10^{-4} radiation length radiator.)

These values scale approximately linearly with distance from the magnet to the dump, and are not very sensitive either to the quadrupole or to small rotations of the exit edge of the tagger magnet. Thus the beam dump design is quite insensitive to the beam optics, and depends only on the lateral and longitudinal spread of the shower in the absorber.

4.5 Polarimetry instrumentation

The majority of bremsstrahlung photons produced in the radiator are absorbed in the collimator system. If the radiator and collimator system are well aligned, the photon spectrum behind the collimators is dominated by the coherent peak. The beam parameters can be determined by using the intensity spectra from the tagger.

Nevertheless, in order to monitor the polarization parameters – degree (P_γ) and direction (ϵ_γ) – of the collimated photon beam it is crucial to have an independent method, either a photon polarimeter detecting the asymmetry of a process that is well understood within theory (QED) or a well known hadronic process so that the measured beam asymmetry can be compared with theoretical (or experimental) expectations. At photon energies above 5 GeV, the forward production of vector mesons is described by vector meson dominance (VMD), resulting in a $sin^2\theta_{hel}cos(2\psi)$ dependence of the vector meson's decay distribution where θ_{hel}, ϕ_{hel} are the polar and azimuthal decay angles in the helicity frame and $\psi = \phi_{hel} - \epsilon_\gamma$. With ρ^0 production accounting for about 10% of all hadronic triggers in the detector, this method suffers no lack of statistics. It is limited only by the accuracy of the VMD approximation, roughly $5 - 10\%$ at these energies.

The other method, measuring the photon polarization by means of a polarimeter, can be realized by a pair polarimeter or a triplet polarimeter. It involves additional hardware components on the beamline between the collimator system and the spectrometer magnet. Both types of polarimeter require a thin radiator and a detector in a field free area followed by a dipole magnet

and counters for the trigger. Space is available upstream of the spectrometer in HALL D for the insertion of a polarimeter.

QED based calculations for the latter process show that the angle and energy of the soft (triplet) electron is almost independent of the energy of the incident photon ($\bar{E}_{triplet} \approx 0.7 - 0.9 MeV$). The low rate of this process and the technical challenge for a counter device measuring accurately the angular distribution of low energy electrons do not favor this type of polarimeter.

For pair production, on the other hand, the opening angle between the produced electron and positron decreases with increasing energy making the measurement more complicated at higher energies. A magnetic separation is not desirable because the deflection cannot be determined very accurately. The proposed polarimeter consists of a thin scintillator ($d = 50\,\mu m$) as an active target, 1.5 m in front of a silicon microstrip detector arrangement, followed by a dipole magnet and two scintillators 10 cm apart from the beamline for triggering on symmetric e^+e^- pairs. The microstrip detector consists of four layers having 512 channels each of silicon wafers with a spatial width for a single channel of 25 μm. The second and third layer are oriented at $\pm 60°$ with respect to the first layer, the fourth perpendicular to one of the previous layers, thus allowing to measure the full angular range of produced e^+e^--pairs without any gap in the acceptance. A Monte Carlo simulation of this device including multiple scattering in the target, the microstrip detector, and foils in the vacuum system (using GEANT) shows that an analyzing power of 25% is achievable (cf. fig 4.24). QED calculations predict an angular distribution for pair production proportional to $(1 + P_\gamma \alpha \cos 2(\phi - \epsilon_\gamma))$ with an analyzing power of $\alpha = 0.28$ for incident photons in the range of 6-10 GeV. Because of the thickness of the microstrip layers (300 μm) it is convenient to measure the beam polarization for fifteen minutes every time the orientation of the crystal radiator or the electron beam parameters have changed. The scintillator target as well as the detector device have to be mounted on motor driven stages so that they can be removed from the beamline.

A research and development program is underway at the Yerevan Physics Institute to test these ideas using the 2 GeV coherent bremsstrahlung beam line at YerPhi (Yerevan, Armenia). This 2-year program is funded by the U.S. Civilian Research and Development Fund, and supports a collaboration of Armenian and U.S. collaborators from the University of Connecticut. One of the primary goals of this project is to show the accuracy with which the polarization of a coherent bremsstrahlung beam can be calculated based upon QED and the measured shape of the intensity spectrum.

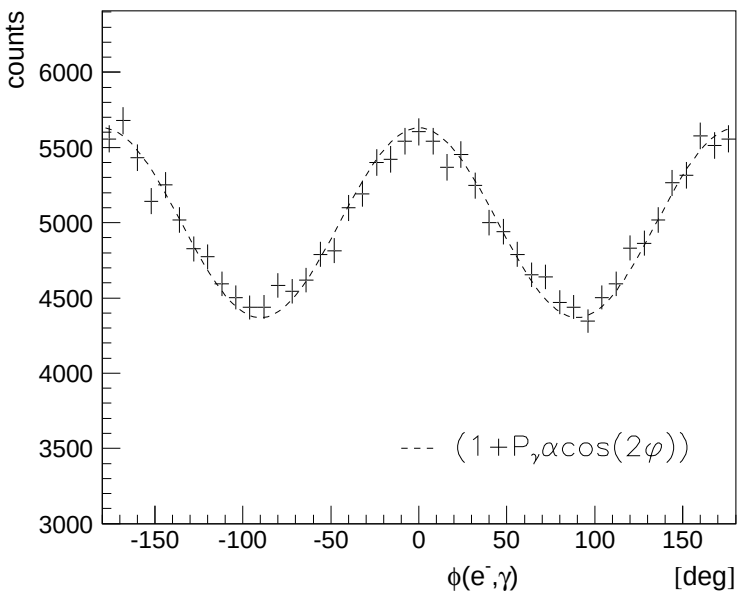

Figure 4.24: Angular distribution for pair production by linearly polarized photons as measured by a polarimeter in comparison with theoretical prediction (*dashed line*). The count rate corresponds to 15 minutes of data taking.

4.6 Operating beam intensity

Table 4.7 brings together the diverse set of parameters that must be considered in evaluating the optimum beam intensity at which an experiment using the coherent bremsstrahlung beam should operate. All four columns of numbers were obtained for the same beam conditions, except that the crystal orientation was adjusted to align the coherent intensity peak at the energy listed in row one. The second row, labeled N_γ, gives the integrated rate of beam photons in the coherent peak downstream of the collimator. Note the sharp decrease in the intensity of the coherent peak as the energy approaches the end point. By contrast, the incoherent bremsstrahlung flux is approximately constant over this range of energies. The third and fourth row show the height and width of the peak in the polarization spectrum of the beam. Rows five and six report the height and width of the peak in the tagging efficiency spectrum. The tagging efficiency is defined as the number of beam photons of a particular energy reaching the target divided by the corresponding rate in the tagging

E of peak	8 GeV	9 GeV	10 GeV	11 GeV
N_γ in peak	185 M/s	100 M/s	45 M/s	15 M/s
peak polarization	0.54	0.41	0.27	0.11
(f.w.h.m.)	(1140 MeV)	(900 MeV)	(600 MeV)	(240 MeV)
peak tagging efficiency	0.55	0.50	0.45	0.29
(f.w.h.m.)	(720 MeV)	(600 MeV)	(420 MeV)	(300 MeV)
power on collimator	5.3 W	4.7 W	4.2 W	3.8 W
power on target	810 mW	690 mW	600 mW	540 mW
total hadronic rate	385 K/s	365 K/s	350 K/s	345 K/s
tagged hadronic rate	26 K/s	14 K/s	6.3 K/s	2.1 K/s

Table 4.7: Operating parameters for an experiment using the coherent bremsstrahlung beam. The calculation assumes a 12 GeV electron beam energy and a 3.4 mm collimator 80 m downstream from a radiator of thickness 10^{-4} radiation lengths. The electron beam current is taken to be 3 μA. The rates in the detector (last two rows) are calculated for a 30 cm liquid hydrogen target and an open hadronic trigger.

focal plane. Large tagging efficiencies are required in order to make effective use of tagging. The width of the peak in the tagging efficiency spectrum determines the width of the focal plane that would be active when running with collimation. The peak integral reported in row two is summed within the f.w.h.m. tagging efficiency window. Rows seven and eight give the photon beam power that is incident on the experimental target (and photon beam dump) and the photon collimator, respectively.

The last two rows in Table 4.7 give the inclusive and tagged rates for hadronic triggers from a 30 cm liquid hydrogen target placed in the beam following the collimator. Note that the total hadronic rate is dominated by background (*i.e.* non-tagged) events associated with the low-energy component of the beam. This is why the total trigger rate is essentially constant while the flux in the coherent peak varies with peak energy over an order of magnitude. This table illustrates the value of having an electron beam energy well above the photon energy needed for the experiment.

List of Figures

4.1 Generic diagrams for hard photon production. 3
4.2 Photon energy spectrum from the Compton back-scatter source 5
4.3 Photon power spectrum from an oriented diamond radiator. . 8
4.4 Schematic plan view of the photon beam line 9
4.5 Coherent bremsstrahlung spectrum 12
4.6 Coherent bremsstrahlung spectrum after collimation. 14
4.7 Linear polarization in the coherent bremsstrahlung peak . . . 16
4.8 Linear polarization of the coherent bremsstrahlung beam . . . 17
4.9 Maximum polarization *vs* radiator-collimator distance. 18
4.10 SRS setup 23
4.11 Rocking curve 1 25
4.12 Rocking curve 2 26
4.13 Collimated coherent bremsstrahlung spectrum 28
4.14 Schematic illustration of crystal mounted in goniometer 29
4.15 Temperature profile of crystal at full current 32
4.16 Coherent photon spectrum 37
4.17 Horizontal and vertical beta functions for electron beam . . . 39
4.18 Horizontal and vertical envelopes for the electron beam 40
4.19 Plan view of tagging spectrometer 44
4.20 Two magnet tagger optics 45
4.21 comparison of beta 46
4.22 Fixed array of tagging counters 50
4.23 Conceptual design of tagging microscope 51
4.24 Angular distribution for pair production by polarized photons 55

List of Tables

4.1 Figure of merit for various materials 19
4.2 Requirements for goniometer axes 30
4.3 Assumed and projected electron beam properties 34
4.4 Tagging spectrometer parameters 45
4.5 Geometry of the tagger 48
4.6 Optical properties of the tagger 49
4.7 Operating parameters for an experiment 56

Bibliography

[1] C. Keppel. Development of a Compton-backscattered photon source for Hall B at Jefferson Lab. In Alex Dzierba, editor, *Physics with 8+ GeV Photons Workshop*, 1997. Workshop in Bloomington IN, July 14-16 1997, proceedings available from Jefferson lab.

[2] W. Kaune, G. Miller, W. Oliver, R.W. Williams, and K.K. Young. Inclusive cross sections for pion and proton production by photons using collimated coherent bremsstrahlung. *Phys. Rev.*, D**11**(3):478–494, 1975.

[3] H. Bilokon, G. Bologna, F. Celani, B. D'Ettorre Piazzoli, R. Falcioni, G. Mannocchi, and P. Picchi. Coherent bremsstrahlung in crystals as a tool for producing high energy photon beams to be used in photoproduction experiments at CERN SPS. *Nuclear Inst. and Meth.*, **204**:299–310, 1983.

[4] G. Diambrini-Palazzi. *Revs. Mod. Phys.*, **40**:611, 1968.

[5] U. Timm. *Fortschr. Phys.*, **17**:765, 1969.

[6] J. Kellie. Private Communication.

[7] C. Sinclair. Private Communication.

[8] J. Benesch. HallD Preliminary Optics Design. Technical Report JLab TN 00-011, Jefferson Lab., 2000.

[9] L. Keller. Muon calculation results. Technical Report HallD Note **33**, SLAC, 2000. `http://www.phys.cmu.edu/halld/notes_main.html`.

[10] D. I. Sober, *et al. Nuclear Inst. and Meth.*, A**440**:263, 2000.

[11] Anthony, *et al. Nuclear Inst. and Meth.*, A**301**:230, 1991.

[12] J. Hall, *et al. Nuclear Inst. and Meth.*, A**368**:689, 1996.